

Deeply Virtual Compton Scattering at 6 GeV with transversely polarized target using the CLAS Detector

H. Avakian^{1, 2}, S. Boyarinov, V.D. Burkert¹, A. Deur, L. Elouadrhiri, D. Gaskell, F-X. Girod, V. Guzey
T. Kageya, V. Koubarovsky, M. Lowry, A. Sandorfi, Yu. Sharabian, S. Stepanyan, X. Wei
Jefferson Lab, Newport News, VA 23606, USA

J. Ball, P.-Y. Bertin, A. El Alaoui, E. Fuchey, M. Garçon, M. Guidal¹, C.E. Hyde, F. Itard,
P. Konczykowski, M. Mac Cormick, B. Michel, B. Moreno, C. Muñoz Camacho, S. Niccolai, B. Pire,
S. Procureur, F. Sabatié¹, S. Wallon, E. Voutier
CPhT Ecole Polytechnique (Palaiseau) / IPN (Orsay) / LPC (Clermont-Ferrand)
LPSC (Grenoble)/ LPT (Orsay) / SPhN (Saclay) CEA/DSM/DAPNIA & CNRS/IN2P3, France
D. Ireland, R. Kaiser¹, I. Lehmann, K. Livingston, D. Protopopescu, G. Rosner, B. Seitz
Univ. of Glasgow, Glasgow G12 8QQ, UK

K. Joo, N. Markov, M. Ungaro, B. Zhao
University of Connecticut, Storrs, CT 06269, USA

P. Rossi, M. Aghasyan, E. De Sanctis, L. Hovsepyan, M. Mirazita, S. Anefalos Pereira
LNF INFN, Frascati, I00044, Rome Italy

A. Biselli
Fairfield University, Fairfield CT 06824, USA

H. Egiyan, M. Holtrop
University of New Hampshire, Durham, NH 03824, USA

S. Kuleshov, O. Pogorelko
Institute of Theoretical and Experimental Physics, Moscow, 117259, Russia

R. Niyazov, P. Stoler
Rensselaer Polytechnic Institute, Troy, NY 12181, USA

M. Amarian, G. Dodge, S.E. Kuhn, A. Radyushkin
Old Dominion University, Norfolk, VA 23529, USA

G.V. Fedotov, B.S. Ishkhanov, E.L. Isupov, V.I. Mokeev, N.V. Shvedunov
Skobeltsyn Institute of Nuclear Physics and Physics Department at Moscow State University
19899 Vorob'evy gory, Skobeltsyn Nuclear Physics Institute at Moscow State University, Moscow, Russia

D. Crabb, S. Liuti, L.C. Smith

¹Co-spokesperson

²Contact person

University of Virginia, Charlottesville, VA 22903, USA
M. Vanderhaeghen
College of William and Mary, Williamsburg, VA 23185, USA

Abstract

We propose to study the spin azimuthal asymmetries in Deep Virtual Compton Scattering (DVCS) using the CEBAF 6 GeV polarized electron beam, a transversely polarized HD-Ice target, and the CEBAF Large Acceptance Spectrometer (CLAS). The main focus of the experiment will be the measurement of the target single spin asymmetry in the reaction $ep \uparrow \rightarrow ep\gamma$. Azimuthal moments in the cross section depend on different combinations of Generalized Parton Distributions (GPDs) and provide access to elusive GPD-E and contributions of u and d quarks to the total orbital angular momentum. The expected asymmetries from the leading-order calculations are in the range of 20 to 40%, depending on the kinematics and on the GPD model used. The Q^2 , x_B , and t dependences of the DVCS amplitude will be studied in a wide range of kinematics. In addition, transverse spin dependent double spin asymmetries (TDSA) for $\vec{ep}^\uparrow \rightarrow ep\gamma$ will be measured simultaneously, giving access to the real part of the target spin dependent DVCS amplitude. A total of 30 days of new beam time is requested for this experiment.

Contents

| | | |
|----------|--|-----------|
| 1 | Introduction | 5 |
| 2 | Theory and motivation | 7 |
| 2.1 | Phenomenology of the GPDs | 7 |
| 2.1.1 | Impact parameter dependent GPDs | 8 |
| 2.2 | Deeply Virtual Compton Scattering | 9 |
| 2.2.1 | GPD studies | 10 |
| 2.2.2 | Target single spin asymmetry. | 11 |
| 2.2.3 | Double spin asymmetry | 13 |
| 3 | Experimental situation | 17 |
| 3.1 | The HERMES Experiment | 17 |
| 3.2 | JLab proposals | 17 |
| 4 | A dedicated DVCS experiment with a transversely polarized target and CLAS | 18 |
| 4.1 | The CLAS configuration | 19 |
| 4.1.1 | CLAS HD Ice transversely polarized target | 19 |
| 4.1.2 | Beam rastering | 20 |
| 4.1.3 | Minitorus magnet as magnetic shield | 21 |
| 4.1.4 | Target polarization measurements | 22 |
| 4.1.5 | Trigger and data acquisition | 25 |
| 4.2 | Event identification, reconstruction, and acceptances | 26 |
| 4.2.1 | Separation of single γ from $\gamma\gamma$ events. | 26 |
| 4.2.2 | $e\gamma X$ studies | 32 |
| 4.3 | Count rates and statistical errors | 32 |
| 4.4 | Systematic errors | 33 |
| 4.5 | Projected results | 35 |
| 5 | Summary and beam time request | 39 |

1 Introduction

In recent years, parton distribution functions have been generalized to contain information not only on the longitudinal but also on the transverse distributions of partons in a fast moving hadron. The generalized parton distributions (GPDs) [1, 2, 3, 4, 5] are the Wigner quantum phase space distribution of quarks in the nucleon – functions describing the simultaneous distribution of particles with respect to both position and momentum in a quantum-mechanical system, representing the closest analogue to a classical phase space density allowed by the uncertainty principle. In addition to the information about the spatial density (form factors) and momentum density (parton distribution), these functions reveal the correlation of the spatial and momentum distributions, *i.e.* how the spatial shape of the nucleon changes when probing quarks and gluons of different wavelengths.

The concept of GPDs has led to completely new methods of “spatial imaging” of the nucleon, either in the form of two-dimensional tomographic images (analogous to Computer Tomography scans in medical imaging), or in the form of genuine three-dimensional images (Wigner distributions). GPDs also allow us to quantify how the orbital motion of quarks in the nucleon contributes to the nucleon spin – a question of crucial importance for our understanding of the “mechanics” underlying nucleon structure. The spatial view of the nucleon enabled by the GPDs provides us with new ways to test dynamical models of nucleon structure.

The detailed understanding of the transverse structure of the nucleon in general and spatial distributions of quarks in particular, have been widely recognized as one of the key objectives of the JLab 12 GeV upgrade project. This requires a comprehensive program, combining results of measurements of a variety of processes in lepton–nucleon scattering with structural information obtained from theoretical studies, as well as with expected results from future lattice QCD simulations.

Deeply Virtual Compton Scattering (DVCS) is one of the key reactions to determine the GPDs experimentally, and it is the simplest process that can be described in terms of GPDs. Measurements of hard exclusive photons, including the Bethe-Heitler, DVCS and their interference (Fig. 1), allow one to separate the imaginary and real parts of the DVCS amplitude by measuring combinations of cross sections and asymmetries with respect to the beam spin (helicity), beam charge (e^+/e^-), and/or target or recoil polarization. The DVCS provides access to combinations of GPDs, so measurements with all possible target polarizations are required to separate contributions of different GPDs [6].

The measurements of the DVCS cross sections and beam spin asymmetries carried out by JLab with 6 GeV beam energy [7] are consistent with the theoretical expectation of dominance of the single-quark reaction mechanism (leading-twist approximation) for DVCS for momentum transfers Q^2 of a few GeV^2 , essential for the GPD interpretation of the $eN \rightarrow e'N\gamma$ data. They also demonstrate the feasibility

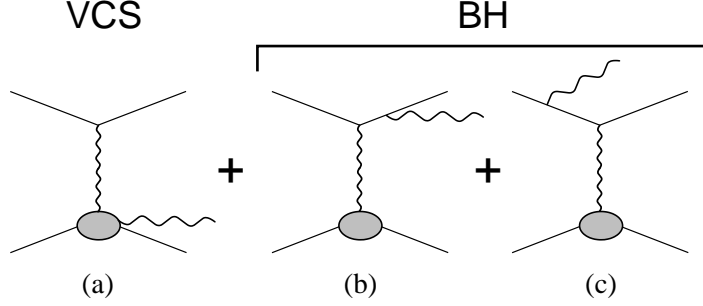


Figure 1: Diagrams contributing to the electroproduction of a real photon. The DVCS process (a) is shown along with the interfering Bethe-Heitler diagrams (b) and (c).

ity of accurate differential measurements of the t -dependence of the cross sections needed for the GPD-based reconstruction of the spatial images of the nucleon. DVCS measurements of the longitudinal target spin asymmetry [8] at Q^2 values as low as 2 GeV^2 , are also consistent with GPD based predictions suggesting that DVCS can be used to extract information about GPDs at the momentum transfers accessible already at JLab.

The DVCS single spin asymmetry for a transversely polarized target (TTSA) is the most sensitive observable to the elusive GPD E , providing access to the orbital angular momentum. Comparison of theory predictions with results on DVCS single spin asymmetries from the HERMES Collaboration for transverse target polarizations [9, 10] indicates great sensitivity of target single spin asymmetries to the contribution of u -quarks to the total angular momentum. The Hall A deuterium DVCS experiment has also demonstrated the sensitivity of the $n(e, e'\gamma)n$ reaction in the impulse approximation to the GPD E [11]. The most sensitive to the GPD- E asymmetry appeared to be the $\cos\phi$ moment of the target (T) spin-dependent contribution for unpolarized beam (U), σ_{UT} [6].

We propose a measurement of DVCS in Hall B at Jefferson Lab with a 6 GeV longitudinally polarized electron beam, transversely polarized HD-Ice target [12], and the CLAS detector while running with high luminosity (2 nA beam current). All possible final state combinations in exclusive photon production, including $epX, e\gamma X$ and $ep\gamma$ will be detected in a wide range of kinematics. Proposed measurements are essential for the study of GPD E , and combined with already approved CLAS measurements with unpolarized and longitudinally polarized targets will allow separation of all helicity conserving (chiral even) leading twist GPDs and constrain the DVCS amplitude in the range of Q^2 from 1 to 4 GeV^2 , and x_B from 0.15 to 0.55. The main goal of this proposal will be the study of the x_B and t dependences of the target Single Spin Asymmetries (SSAs).

The CLAS detector with the proposed configuration, including the polarized target and a 6 GeV longitudinally polarized electron beam form a unique facility to perform such measurements with a single experimental setup in a wide range of kinematics.

2 Theory and motivation

2.1 Phenomenology of the GPDs

GPDs unify the momentum-space parton densities measured in inclusive deep-inelastic eN scattering with the spatial densities (form factors) measured in eN elastic scattering. They describe correlations between the momentum and spatial distributions of quarks, which are revealed in exclusive processes in eN scattering at large momentum transfer (deeply virtual Compton scattering, meson production). They depend on the fractions of the nucleon momentum carried by the quark before and after the process, $x+\xi$ and $x-\xi$ (ξ defines the longitudinal momentum transfer to the nucleon, $2\xi \approx x_B/(2-x_B)$), as well as on the momentum transfer to the nucleon, t (Fig.2). The presence of spin – both of the nucleon and the quark – as well as quark flavors (u, d, s) lead to the appearance of various independent spin/flux components of the GPDs.

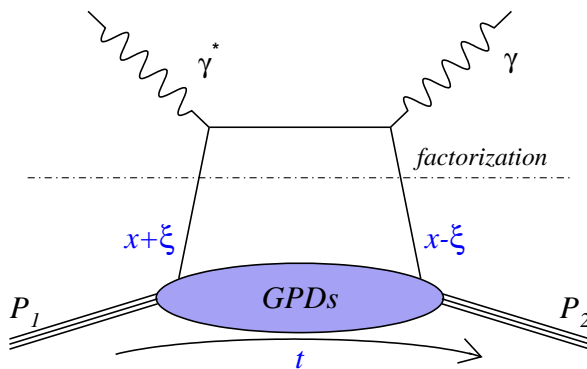


Figure 2: Handbag diagram for DVCS. t is the squared 4-momentum transfer to the proton, x is the average longitudinal momentum fraction, in terms of $(p+p')/2$, of the active quark in the initial and final states, and $2\xi \approx x_B/(2-x_B)$ parameterizes the difference.

The GPD application became apparent after it had been shown [3, 2, 13] that measurements of the second moment of the sum of the ‘unpolarized’ GPDs H and E open, for the first time, access to the gravitational form factors $J^q(t)$, $M^q(t)$ and $d(t)$ of the energy-momentum tensor for partons inside a hadron :

$$J^q(t) = \frac{1}{2} \int_{-1}^1 dx x [H^q(x, \xi, t) + E^q(x, \xi, t)] \quad (1)$$

$$M^q(t) + \frac{4}{5}d(t)\xi^2 = \frac{1}{2} \int_{-1}^1 dx x H^q(x, \xi, t) \quad (2)$$

where $J^q(t)$, $M^q(t)$ and $d(t)$ respectively give access to the distributions of angular momentum, mass and forces inside the hadron.

In this relation $H^q(x, \xi, t)$ and $E^q(x, \xi, t)$ denote parton spin non-flip and spin flip GPDs ($q = u, d, s$), respectively.

There are four independent quark-helicity conserving GPDs: H, \tilde{H}, E , and \tilde{E} for each quark flavor q and four “transversity” (chiral-odd) GPDs H_T, \tilde{H}_T, E_T , and \tilde{E}_T . While for chiral-even GPDs currently quite a few processes have been under intensive study, there are very few suggestions on how to access experimentally “transversity” GPDs [14, 15, 16, 17]. For the time being the lattice calculations remain the only source of information [18].

2.1.1 Impact parameter dependent GPDs

The impact parameter dependent GPDs are defined as the two-dimensional Fourier transform of the GPD (for $\xi = 0$), with respect to transverse momentum transfer, Δ_\perp , describing the distributions of quarks with longitudinal momentum fraction x over the transverse distance, \vec{b}_T , from the center of the nucleon (impact parameter). The integral of this spatial distribution over \vec{b}_T gives the total parton density at a longitudinal momentum fraction x . This 1+2-dimensional “mixed” momentum and coordinate representation corresponds to a set of “tomographic images” of the quark distribution in the nucleon at fixed longitudinal momentum, x .

Quark density distributions in the transverse plane for different combinations of transverse spin of proton and quark [18] are shown in Fig.3.

The probability density of finding an unpolarized quark with longitudinal momentum fraction x at transverse position \vec{b}_T inside a transversely polarized nucleon is given by:

$$\mathcal{F}^q(x, \vec{b}_T; S) = \mathcal{H}^q(x, \vec{b}_T^2) + \frac{(\hat{P} \times b_T) S_T}{M} \left(\mathcal{E}^q(x, \vec{b}_T^2) \right)', \quad (3)$$

where S parametrizes all possible combinations of the helicities λ and λ' as described in Refs. [19, 20] and S_T is the transverse polarization. The GPDs \mathcal{H}^q and \mathcal{E}^q are the Fourier transformed GPDs H^q and E^q , respectively, and the prime denotes the first derivative with respect to \vec{b}_T^2 .

Similar to the GPDs in impact parameter space the transverse momentum dependent parton distributions (TMDs) [21] have a probability interpretation, too. The probability of finding an unpolarized quark with longitudinal momentum fraction x and transverse momentum \vec{k}_T inside a transversely polarized target is given by:

$$\Phi^q(x, \vec{k}_T; S) = f_1^q(x, \vec{k}_T^2) - \frac{(\hat{P} \times k_T) S_T}{M} f_{1T}^{\perp q}(x, \vec{k}_T^2), \quad (4)$$

where f_1^q is the standard unpolarized quark distribution function and f_{1T} is the Siverson distribution function defining the probability to find unpolarized quarks in the transversely polarized nucleon.

A relation has been derived [22, 19, 20] between the GPD-E and the Sivers TMD linking the derivative of the GPD-E with Sivers distribution function. It was shown that in some simple spectator models (a scalar diquark spectator model of the nucleon and a quark target model in perturbative QCD) that relations hold to lowest order in perturbation theory [20]. Global analysis of hard exclusive (accessing GPDs) and semi-inclusive processes (accessing TMDs) will provide tests of these relation.

2.2 Deeply Virtual Compton Scattering

The most favorable physical observables to unravel GPDs from cross sections are spin-azimuthal asymmetries. These asymmetries allow us to extract separate components of the angular dependence of the cross section and, in this manner, to project out distributions carrying information on the orbital momentum of constituents in the nucleon.

In the $eN \rightarrow eN\gamma$ cross section, the DVCS amplitude interferes with the known amplitude of the Bethe-Heitler (BH) process, in which the final-state photon is emitted from the electron (see Fig. 1). The total cross section is given by [6]:

$$\frac{d\sigma^{ep \rightarrow ep\gamma}}{dx_B dy d\Delta^2 d\phi} = \frac{\alpha^3 x_B y}{16\pi^2 Q^2 \sqrt{1+\epsilon^2}} \left| \frac{\mathcal{T}}{e^3} \right|^2, \quad (5)$$

where $\epsilon = 2x_B M/Q$, y is the fraction of the electron energy lost in the nucleon rest frame and ϕ (Fig.4) is the angle between the leptonic plane (e, e') and the photonic plane ($\gamma^*(q_1), \gamma(q_2)$).

The total amplitude \mathcal{T} is the superposition of the BH and DVCS amplitudes:

$$|\mathcal{T}|^2 = |\mathcal{T}_{BH}|^2 + |\mathcal{T}_{DVCS}|^2 + \mathcal{I} \quad (6)$$

$$\mathcal{I} = \mathcal{T}_{DVCS}^* \mathcal{T}_{BH} + \mathcal{T}_{DVCS} \mathcal{T}_{BH}^*, \quad (7)$$

where \mathcal{T}_{DVCS} and \mathcal{T}_{BH} are the amplitudes for the DVCS and Bethe-Heitler processes, and \mathcal{I} denotes the interference between these amplitudes.

The individual contributions to the total $ep \rightarrow ep\gamma$ cross section can be written (up to twist-3 contributions) [6] as:

$$|\mathcal{T}_{BH}|^2 = \frac{\Gamma_{BH}(x_B, Q^2, t)}{\mathcal{P}_1(\phi) P_2(\phi)} \left\{ c_0^{BH} + \sum_{n=1}^2 c_n^{BH} \cos(n\phi) + s_1^{BH} \sin \phi \right\}, \quad (8)$$

$$|\mathcal{T}_{DVCS}|^2 = \Gamma_{DVCS}(x_B, Q^2, t) \left\{ c_0^{DVCS} + \sum_{n=1}^2 [c_n^{DVCS} \cos(n\phi) + s_n^{DVCS} \sin(n\phi)] \right\},$$

$$\mathcal{I} = \frac{\Gamma_I(x_B, Q^2, t)}{\mathcal{P}_1(\phi) P_2(\phi)} \left\{ c_0^I + \sum_{n=1}^3 [c_n^I \cos(n\phi) + s_n^I \sin(n\phi)] \right\}, \quad (9)$$

where $\mathcal{P}_1(\phi)$ and $\mathcal{P}_2(\phi)$ are the BH electron propagators, $\Gamma_{BH}, \Gamma_{DVCS}, \Gamma_I$ are known kinematic factors, and c_i, s_i are azimuthal moments in the corresponding cross section contributions.

Depending on whether the beam helicity or target spin is flipped, different GPD contributions enter the cross section azimuthal moments ($\sigma_{LU}, \sigma_{UL}, \sigma_{UT}$). For the transversely polarized target, all harmonics also depend on the angle $\phi_S - \phi$, where ϕ_S is the azimuthal angle of the transverse spin.

The Fourier coefficients in $|\mathcal{T}_{BH}|^2$ are calculable in QED, while the ones appearing in \mathcal{I} and $|\mathcal{T}_{DVCS}|^2$ depend on so-called Compton form-factors (CFF). At twist-2 level, some of the higher Fourier coefficients are zero, and four CFFs ($\mathcal{H}, \tilde{\mathcal{H}}, \mathcal{E}, \tilde{\mathcal{E}}$) describe the process; these CFF are complex quantities, directly related to the four twist-2 GPDs by:

$$\Re \mathcal{H} = \sum_q e_q^2 P \int_{-1}^{+1} \left[\frac{1}{\xi - x} - \frac{1}{\xi + x} \right] H^q(x, \xi, t) dx \quad (10)$$

$$\Im \mathcal{H} = \pi \sum_q e_q^2 [H^q(\xi, \xi, t) - H^q(-\xi, \xi, t)] \quad (11)$$

and similarly for the three other CFFs.

The four Compton form factors (CFFs), $\mathcal{H}, \mathcal{E}, \tilde{\mathcal{H}}, \tilde{\mathcal{E}}$ directly accessible from the experiment are given by a convolution of perturbatively calculable coefficient functions and corresponding twist-two GPDs [6]. Eight observables, namely the first harmonics $\cos(\phi)$ and $\sin(\phi)$ of the interference term, are accessible in polarized beam and target experiments, providing access to the real and imaginary parts of all four CFFs. Thus, experiments with both longitudinally and transversely polarized target can measure all eight Fourier coefficients $c_{1,A}^{\mathcal{I}}$ and $s_{1,A}^{\mathcal{I}}$ and with $A = \{\text{unp}, \text{LP}, \text{TP}_x, \text{TP}_y\}$. Extraction of the CFFs using measured azimuthal moments $c_{1,A}^{\mathcal{I}}$ and $s_{1,A}^{\mathcal{I}}$ is straightforward, once all four asymmetries (beam, longitudinal and 2 transverse) are measured (APPENDIX A)[6].

2.2.1 GPD studies

Studies of DVCS and in particular hard meson production processes will require a combination of high energy and high intensity beam, and are generally much more challenging than traditional inclusive scattering experiments. DVCS is the most promising channel for studying GPDs at lower energies and Q^2 . The handbag diagram (see Fig. 2) is expected to dominate at lower Q^2 than in the case of deep exclusive meson production.

The different nucleon spin components of the GPDs can be extracted by measuring target spin asymmetries. Measurements of the t (Δ_{\perp}) dependence provide the information necessary for transverse nucleon imaging. Information about the flavor decomposition requires measurements with both protons and neutrons. Additional

information about the spin/ flavor separation can come from meson production data. The most sensitive to the GPD- E asymmetry appeared to be the $\cos\phi$ moment of the spin-dependent contribution σ_{UT} [6],

$$\sigma_{UT}^{\cos\phi} \sim \frac{1-x}{2-x} \frac{t}{M^2} F_2 \mathcal{H} + \frac{t}{4M^2} (2-x) F_1 \mathcal{E}. \quad (12)$$

Transverse target DVCS SSA measurements in addition to beam spin-dependent SSAs and longitudinally polarized target SSA measurements, thus provide the full set of data needed for the extraction of Compton form factors and corresponding GPDs. The Transverse Target Spin Asymmetry (TTSA) A_{UT} is especially sensitive to the GPD E , and as such will constrain any extraction of the angular momentum J .

The quark angular momentum in the nucleon, J_q , can be estimated if one uses the results of measurements of DVCS observables with different target polarizations to constrain GPD parameterizations, which incorporate information about GPDs obtained from other processes (inclusive DIS, form factors). The accurate measurements of the asymmetries with proton and deuteron targets will be able to constrain J_q in this way.

A full program to extract GPDs from measurements requires coverage of a large kinematic range in x_B , t , and Q^2 , along with measurements of several final states together with the use of polarized beam and polarized targets (both longitudinal and transverse polarizations).

2.2.2 Target single spin asymmetry.

The target SSA arising from interference of DVCS and Bethe-Heitler is sensitive to twist-2 GPDs and its azimuthal dependence is given by a combination of different harmonics of ϕ and ϕ_S (see Fig.4), giving access to imaginary and real parts of corresponding Compton Form Factors $\mathcal{H}, \mathcal{E}, \tilde{\mathcal{H}}, \tilde{\mathcal{E}}$ (CFFs). Separation of different combinations of azimuthal moments in ϕ and ϕ_S appearing in the cross section require a 2-dimensional analysis of moments in the ϕ and ϕ_S plane. This makes the transverse target data analysis very different from simple $\sin\phi$ moment extractions used for SSA studies in DVCS with unpolarized and longitudinally polarized targets. Different observable asymmetries proposed to access GPDs include $A_{UT_x}(\phi)$ and $A_{UT_y}(\phi)$ (VGG [23]) or $A_{UT}^{\sin(\phi_S-\phi)\cos(\phi)}$ and $A_{UT}^{\sin(\phi_S-\phi)\sin(\phi)}$ (BMK [6]) which are in first approximation linear functions of CFFs with a dominant contribution from $\Im\mathcal{H}$ and $\Im\mathcal{E}$, and from $\Im\tilde{\mathcal{E}}$ and $\Im\tilde{\mathcal{H}}$, respectively, along the lines $x = \pm\xi$ [24].

Two different sets of parameterizations were used to make predictions for expected effects. In order to constrain the GPDs, the transverse polarization component of the interference term, \mathcal{I}_{TP} , has to be singled out. This can be accomplished by forming

the transverse (T) target-spin asymmetry with unpolarized (U) beam:

$$\begin{aligned}
A_{UT}(\phi_S - \phi) &= \frac{d\sigma(\phi_S - \phi) - d\sigma(\phi_S - \phi + \pi)}{d\sigma(\phi_S - \phi) + d\sigma(\phi_S - \phi + \pi)} \\
&\simeq A_{UT}^{\sin(\phi_S - \phi) \cos \phi} \cdot \sin(\phi_S - \phi) \cos \phi \\
&\quad + A_{UT}^{\cos(\phi_S - \phi) \sin \phi} \cdot \cos(\phi_S - \phi) \sin \phi.
\end{aligned} \tag{13}$$

The projections for $A_{UT}^{\sin(\phi_S - \phi) \cos \phi}$ and $A_{UT}^{\cos(\phi_S - \phi) \sin \phi}$ are calculated for different values of the total angular momentum J_u . Since the contributions of u -quark and d -quark are proportional to the corresponding squared charge, the d -quark contribution is suppressed and hence in the projections a fixed value is used for J_d .

Variations in the parameter settings for the GPD E become manifest in $A_{UT}^{\sin(\phi_S - \phi) \cos \phi}$ while $A_{UT}^{\cos(\phi_S - \phi) \sin \phi}$ shows only minor modifications. In projection plots for simplicity the symbol A_{UT} is used for $A_{UT}^{\sin(\phi_S - \phi) \cos \phi}$ defined (see APPENDIX-B for more details) as

$$A_{UT}^{\sin(\phi_S - \phi) \cos \phi} = \frac{1}{\pi} \int_0^{2\pi} d\phi \cos \phi A_{UT}^{\sin(\phi_S - \phi)}(\phi). \tag{14}$$

Figures 5 - 6 show the asymmetry for proton, neutron and deuteron targets respectively, plotted as a function of contributions of u and d -quarks to the orbital angular momentum (J_u, J_d) calculated using the Dual parameterization of GPDs H and E from Refs.[25].

Using both Regge and factorized ansätze, the asymmetries are calculated for different possible cases. Calculations show very significant variations of azimuthal distributions on the values of J_u and J_d (see Fig.24). Within these model calculations $A_{UT}^{\sin(\phi_S - \phi) \cos \phi}$ turns out to be sizable even when the calculation is done for $E_q = 0$. Thus a solid knowledge about the GPD H_u is needed in order to constrain J_u . The model parameters for the GPD H_u , can be well constrained by the dedicated DVCS measurements at CLAS and Hall-A, using an unpolarized and longitudinally polarized hydrogen targets. Since in addition the profile parameters are assumed to be the same for the GPD E_u , the only remaining free parameter is J_u . Hence the projected measurement of $A_{UT}^{\sin(\phi_S - \phi) \cos \phi}$ has a clear potential to constrain J_u , as can be seen from Figures 5 - 6.

At our typical kinematics ($x_B \approx 0.3$), A_{UT} has sensitivity to all four GPDs and therefore, combined with unpolarized and longitudinally polarized DVCS asymmetries will provide a complete set of measurements to extract different contributions.

The projection curves for CLAS running with a transversely polarized target have been calculated assuming a luminosity of $5 \times 10^{33} \text{cm}^{-2} \text{s}^{-1}$, with a $HD - Ice$ target polarization of 75% for hydrogen and 25% for deuterium with 25 days of data taking.

Transverse target DVCS SSA measurements in addition to beam SSA from unpolarized target [26] and longitudinally polarized target SSA measurements will provide a set of data needed for the extraction of CFFs and

corresponding GPDs. A_{UT} is especially sensitive to the GPD E , and as such will constrain any extraction of the angular momentum J .

2.2.3 Double spin asymmetry

With the use of a polarized electron beam, this experiment will also determine the double spin asymmetry A_{LT} . Certain moments of the TTSA will provide access also to real part of CFFs, the double spin asymmetries, however provide bigger variety of observables sensitive to the real part of corresponding CFFs. At twist-2 level, this observable takes the form:

$$A_{LT}(\phi) \sim \frac{c_{0,TP}^{BH} + c_{0,TP}^{\mathcal{I}} + (c_{1,TP}^{BH} + c_{1,TP}^{\mathcal{I}}) \cos(\phi) + (s_{1,TP}^{BH} + s_{1,TP}^{\mathcal{I}}) \sin(\phi)}{c_{0,unp}^{BH} + \dots} \quad (15)$$

As in the case of A_{UT} , more interesting object is the $\sin(\phi_S - \phi)$ moment of the asymmetry $A_{LT}^{\sin(\phi_S - \phi)}(\phi)$ (more details in APPENDIX) defined as,

$$A_{LT}^{\sin(\phi_S - \phi) \sin \phi} = \frac{1}{\pi} \int_0^{2\pi} d\phi \sin \phi A_{LT}^{\sin(\phi_S - \phi)}(\phi) \quad (16)$$

The A_{LT} (used for simplicity in projection plots) exhibits a measurable sensitivity to $\Re\mathcal{H}$ and $\Re\mathcal{E}$. Measurements with both beam and target polarized provides a unique possibility to access real parts of CFFs through measurements of spin asymmetries.

The polarized electron beam is also needed for the measurement of the target polarization through $\vec{e}p\uparrow$ elastic scattering (see Section 4.1.1). Unlike A_{LU} , the Bethe-Heitler process alone can generate a double spin asymmetry A_{LT} .

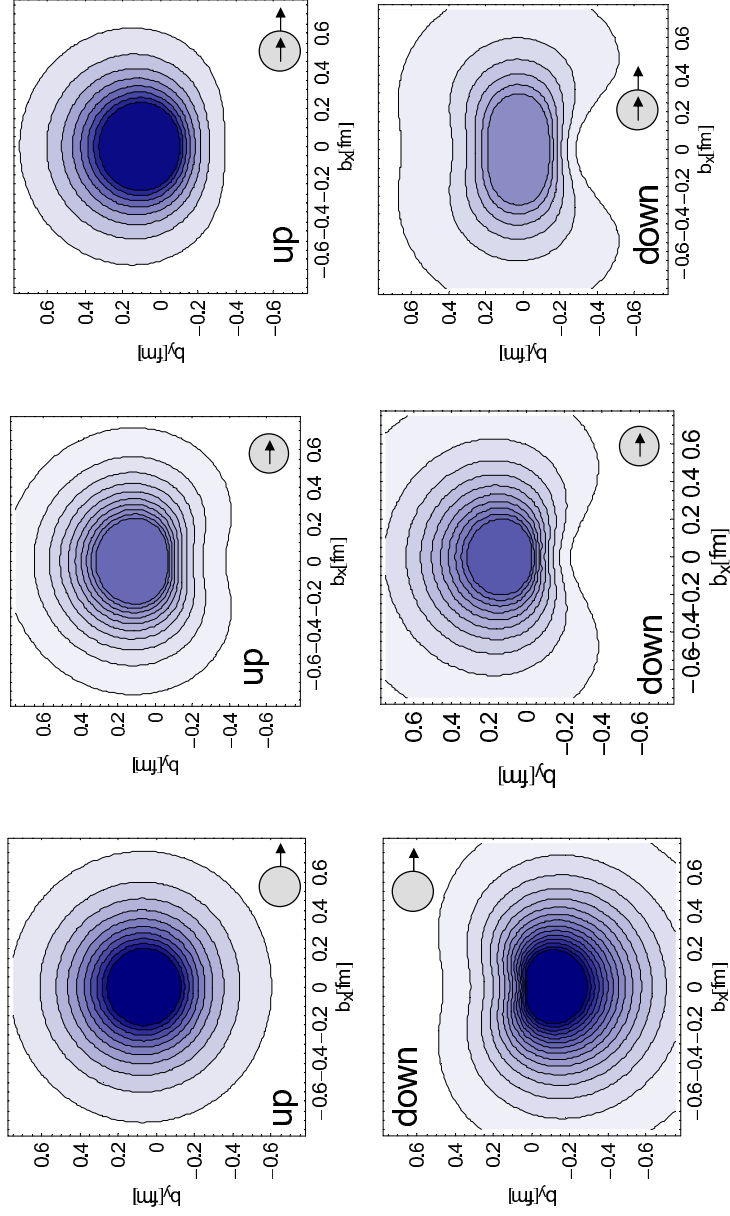


Figure 3: Density distributions for different combinations of proton (outer arrow) and quark (inner arrow) spin. The bottom plot shows density distributions of unpolarized quarks in the transversely polarized nucleon defined by the GPD-E. Other 2 sets of distributions are defined by “transversity” GPDs [18].

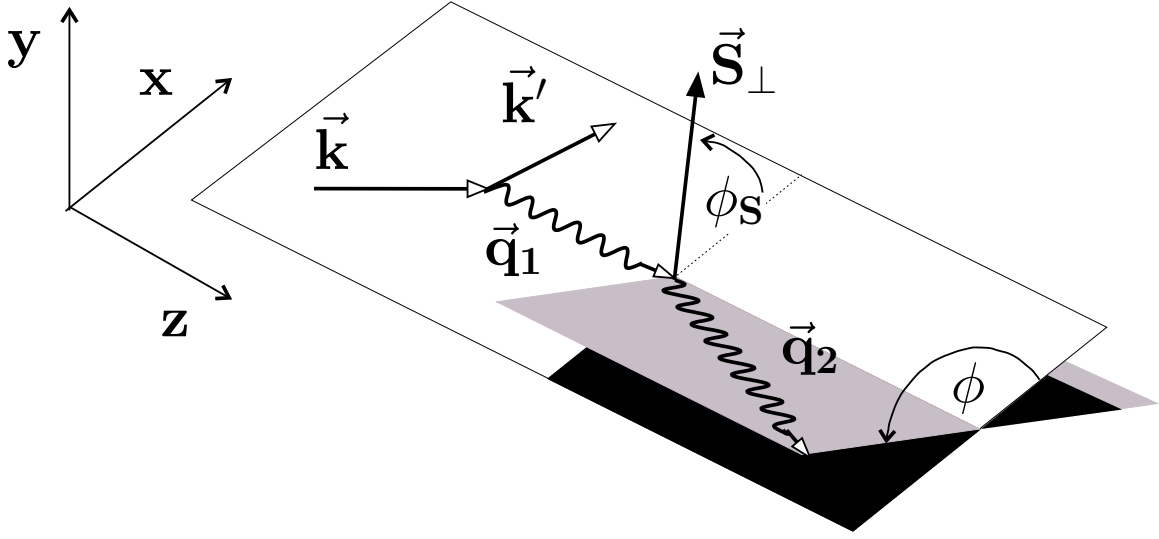


Figure 4: The DVCS kinematics

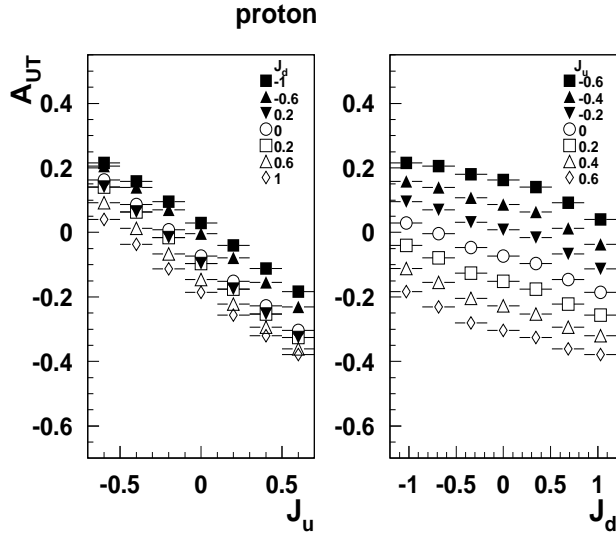


Figure 5: The $A_{UT}^{\cos \phi}$ for a proton target for different values of J_u and J_d ($x = 0.35, Q^2 = 2.5, t = -0.55$).

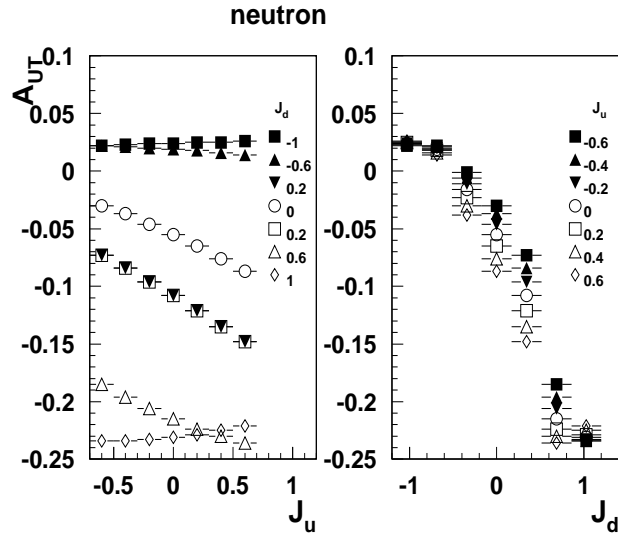


Figure 6: The $A_{UT}^{\cos \phi}$ for a proton target for different values of J_u and J_d ($x = 0.25, Q^2 = 2.0, t = -0.55$).

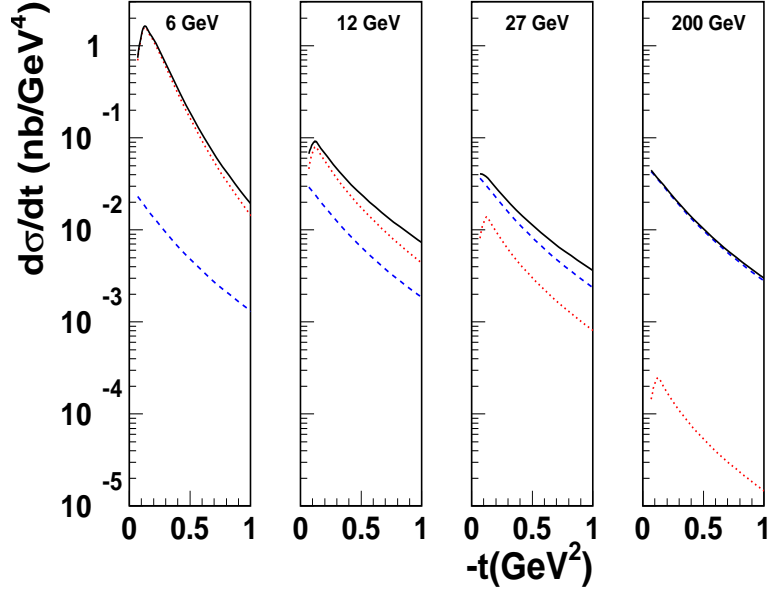


Figure 7: DVCS and BH cross sections for different beam energies.

3 Experimental situation

3.1 The HERMES Experiment

Preliminary target spin asymmetries have been shown by the HERMES Collaboration on the proton [9, 10]. No DVCS data is available currently for the transversely polarized deuteron target. Due to significantly higher BH cross section in the CLAS kinematics (Fig. 7), the statistics at $x_B > 0.2$ will exceed HERMES data by an order of magnitude.

3.2 JLab proposals

No other proposals at the Jefferson Laboratory are available for the study of the DVCS process with transversely polarized target.

CLAS, together with the CEBAF 6-GeV high-polarization beam is uniquely positioned to perform exploratory measurements of deep exclusive reactions in the valence region, with a polarized target especially for DVCS.

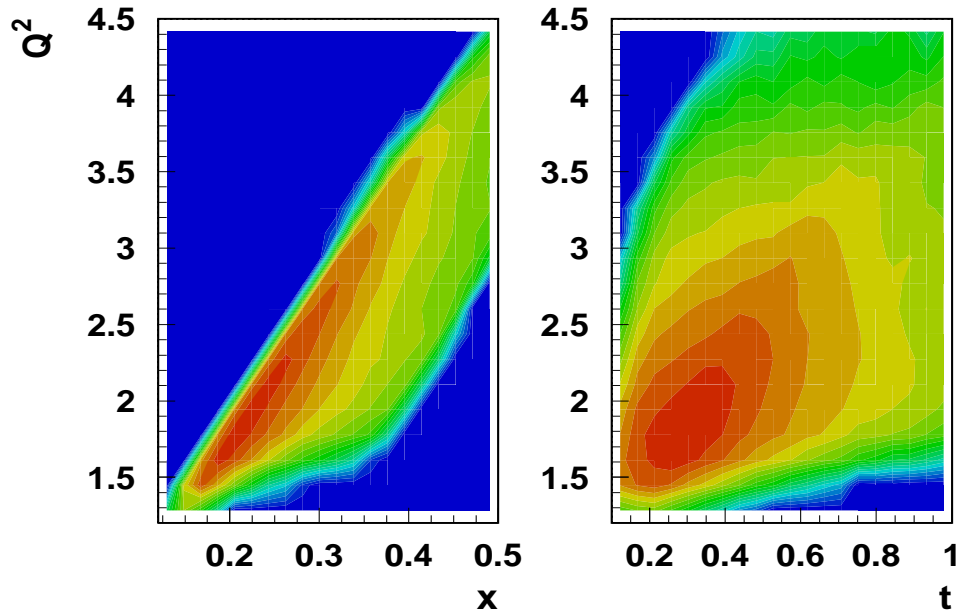


Figure 8: The kinematic coverage in Q^2 , x and t .

4 A dedicated DVCS experiment with a transversely polarized target and CLAS

The main goal of the proposed experiment is to measure the t and x_B dependences of the target single spin asymmetries (TTSA or A_{UT}) in accessible kinematics (see Figure 8).

The target single spin asymmetry (target SSA or A_{UT}) will be calculated as:

$$A_{UT} = \frac{1}{f P_T} \frac{(N_{\gamma}^{+} - N_{\gamma}^{-})}{(N_{\gamma}^{+} + N_{\gamma}^{-})} \quad (17)$$

where P_T is the target polarization, f is the dilution factor, and $N_{\gamma}^{+(-)}$ is the extracted number of $ep \uparrow \rightarrow ep\gamma$ events for opposite orientations of the transverse spin of the nucleon.

We will also obtain the double spin asymmetry (TDSA or A_{LT}) for the same x_B and t bins. These quantities are directly sensitive to the model descriptions of the GPDs. This experiment will be the first statistically significant measurements of the

kinematic dependences of the target TTSA and the TDSA in the DVCS process in the valence region.

A_{UT} will be measured as defined in Eq. 17 and A_{LT} will be measured as:

$$A_{LT} = \frac{1}{fP_eP_T} \frac{(N_{\gamma}^{+\uparrow} + N_{\gamma}^{-\downarrow}) - (N_{\gamma}^{+\downarrow} + N_{\gamma}^{-\uparrow})}{(N_{\gamma}^{+\uparrow} + N_{\gamma}^{-\downarrow}) + (N_{\gamma}^{+\downarrow} + N_{\gamma}^{-\uparrow})} \quad (18)$$

where P_e is the electron beam polarization, and $N_{\gamma}^{\pm\uparrow\downarrow}$ is the extracted number of $\vec{e}p^{\uparrow} \rightarrow ep\gamma$ events for positive or negative helicities of the beam electrons and target polarizations.

4.1 The CLAS configuration

4.1.1 CLAS HD Ice transversely polarized target

The strong holding fields accompanying transversely polarized target employing dynamical polarization methods can deflect the electron beam and create challenging background conditions. A magnetic chicane is typically being installed upstream of the target and arranged in such a way that the target's magnetic field bends the electron beam back on axis [27]. However, bremsstrahlung created in the target material will be peaked along the direction of the incoming electrons, which will then be at several degrees to the detector axis depending on the holding field.

Generally, one can arrange to have either the electron beam or the target bremsstrahlung centered at 0° , but not both. A transversely polarized target in a frozen-spin state, such as the HD-Ice target, requires only small holding fields, and greatly mitigates such background problems. Problems associated with beam deflection are virtually eliminated by the small holding fields and this potentially allows the target to be located even in the center of the detector, thus dramatically increasing the acceptance. In addition, the HD-Ice target has almost no dilution compared to standard solid state targets.

The composition for a 4cm HD-Ice target is shown in the Table 4.1.1

Table 1: HD-Ice materials.

| Material | gm/cm ² | mass fraction (%) |
|----------|--------------------|-------------------|
| HD | 0.735 | 77% |
| Al | 0.155 | 16% |
| CTFF | 0.065 | 7% |

The only unpolarizable nucleons are associated with the target cell and these can be sampled and subtracted in conventionally empty-cell measurements. At the same time, the low Z results in a long radiation length and comparatively few bremsstrahlung photons.

The HD-Ice target developed at LEGS in Brookhaven and now migrating from BNL to JLab, has been used quite successfully in photon beam experiments. The factors affecting target polarization are complex and intertwined; a direct test of the performance of polarized HD with electrons is essential. This will be carried out during the course of the E06-101 run [12].

At BNL, HD target polarizations of 60% H and 35% D have been used in photon experiments with spin-relaxation times in excess of a year, and polarizations are expected to be higher (75% H and 40% D) with the smaller diameter cells that will be used at JLab. The deuterium polarization is particularly stable; spin-relaxation times of 2 months have been measured with only 0.01 T (100 gauss) holding field and 0.2 K. The projected D-decay time for a 0.04 T saddle coil, 0.12 m in length ($BdL \approx 0.005$ T-m), is 7 months. Comparable H relaxation times require higher fields but should be possible with $BdL = 0.050$ Tm, which is still about 30 times less than a dynamically polarized ammonia target. The beam heating expected from 5 nAmps of 6 GeV electrons traversing a 4 cm HD target is ~ 10 mW (as calculated with GEANT). This is about the cooling power of the existing BNL In-Beam-Cryostat (IBC) at 0.5 K and will be significantly increased in the CLAS-IBC now under design for E06-101. Beam heating is considerably less in HD, as compared to Butanol, due to the lower Z and, unlike Butanol, HD relaxation times are not so strong functions of temperature so that long life-times are achievable up to about 0.7 K. Free radicals generated by electron bremsstrahlung will have randomly oriented polarizations. While their absolute number is small, they can generate polarization sinks within the target if the spin-diffusion time is short. This time constant has been indirectly measured at BNL by using RF to punch a local polarization hole within a highly polarized target. The rate at which this hole heals after the RF power is lowered reflects the in-diffusion of spin from other regions of the target. At 2 K, this measured spin-diffusion is 1 day for H but unmeasurably long for D (greater than a year). How much the H performance improves at lower temperatures is a matter for further study, but the extremely slow spin-diffusion for D already suggests that frozen-spin HD could maintain its deuterium polarization during electron experiments. Frozen-spin HD-Ice, thus, provides a very attractive alternative for electron experiments in particular with transversely polarized targets.

4.1.2 Beam rastering

To avoid radiation damage to the target the beam will be rastered over the target surface in a spiral pattern. The beam position is measured indirectly by recording the simultaneous currents of the raster magnet. These values can be used off-line to correct for effects of the raster on the vertex z -position. Figure 9 shows the z -vertex position before and after correction for polarized target data set.

The raster magnets may be also used to give a small angle ($\sim 0.2^\circ$) to the incident electron beam, so that beam at target center will be collinear with the z -axis to confine

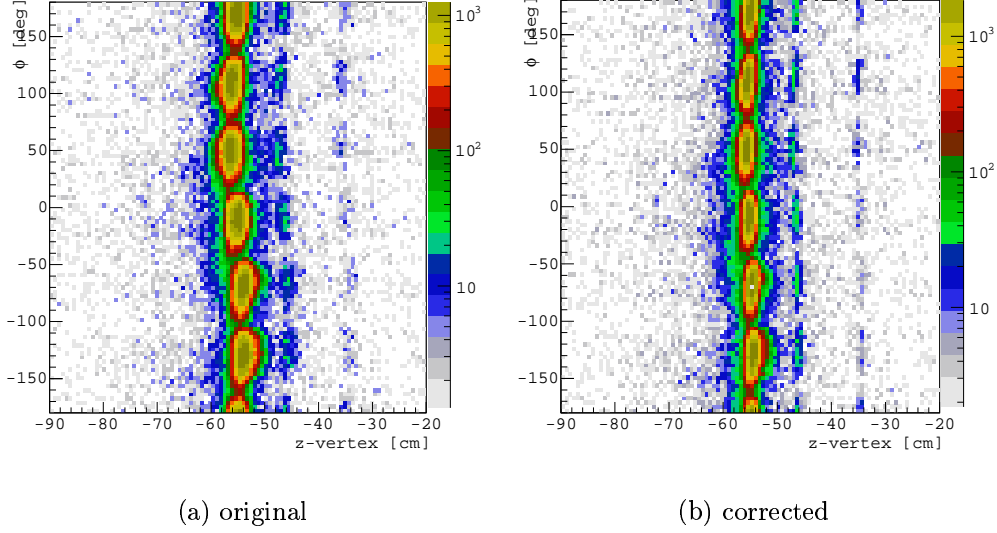


Figure 9: Electron z-vertex position for eg1b data before and after the raster corrections

BH photons in the beam pipe. The deflection of the primary beam by the target field will be fixed by a compensation coil or upstream magnets located in region III of CLAS. The Figure 10 shows the CLAS setup with transversely polarized target at $z=-70$ cm and minitorus at $z=-50$ cm.

4.1.3 Minitorus magnet as magnetic shield

One of the main sources of background produced by a high-energy electron beam impinging upon a HD target is due to interactions of the electron beam with the atomic electrons (Møller scattering). This rate is several orders of magnitude larger than the inelastic hadronic production rate. In case of the HD-Ice target with low holding field CLAS minitorus magnet will be used to direct Møller electrons, so they will be absorbed in the downstream shielding pipe (Fig. 10).

The relative position of the minitorus and the target with respect to the CLAS center will be optimized using the GSIM. The background rates due to Møller electrons are relatively small due to low density of the target and low current, which will be mainly limited by the target capability to keep the polarization.

Shifting the target upstream will significantly increase the kinematic coverage for the direct detection of high-energy photons, the ones from the DVCS process as well as those coming from the decay of high momentum π^0 s. The reconstruction efficiency as a function of the azimuthal angle ϕ and momentum transfer t is shown in Fig. 11.

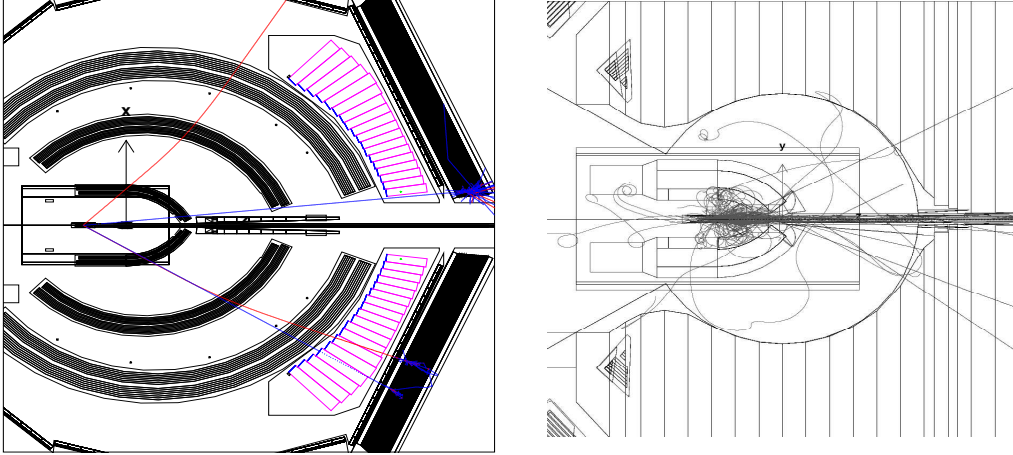


Figure 10: CLAS setup with HD-Ice target positioned at -70 cm. Minitorus positioned at -50 cm. A single DVCS event shown in CLAS (left) and Moller electrons in the field of minitorus (right)

4.1.4 Target polarization measurements

There are four possible transverse combinations: (1) H and D both up, (2) H up/D down, (3) H down/D up, (4) H and D both down. Using the RF flipping of spins, one can switch between (1) and (4) or between (2) and (3) by simply rotating the field. The spins will follow, and this has 100% efficiency. Possible options include both H and D polarized as well as one of them unpolarized.

The In-Beam-Cryostat that will hold HD targets within the CLAS will have a short saddle coil wound on top of a long solenoid. The saddle coil will maintain transverse spin orientations. Keeping this coil short will both reduce the BdL deflection of electrons as well as minimize spin diffusion from radiation damage (by changing the Larmor frequency across the target). However, the fields associated with this coil will be too non-uniform for NMR measurements. Instead, the solenoid will be used for NMR polarization monitoring. The target spins will readily follow the field as the solenoid is energized and the saddle coil is ramped down. NMR data will be collected at the fields matching the Larmor frequencies, typically 0.15 T for H and 0.9 T for D, after which the saddle coil will be ramped up and the solenoid ramped down. We anticipate a total cycle time of about 15 minutes (limited by how fast fields can be changed without quenching the magnets), enabling NMR data to be collected several times a day. If the expected in-beam lifetimes with electrons on HD are more than the several days needed for a viable experiment, this should be more than sufficient.

For nuclear targets, a crossed coil NMR polarimeter, with a pair of coils arranged with orthogonal axes and a pair of associated resonant circuits, monitors nuclear polarization in HD [28]. With an external magnetic field, low-power RF on the transmitter coil samples polarization by flipping a small fraction ($< 10^{-5}$) of spins, which induces a current in the receiver coil. The sensitivity of the circuit to polarization

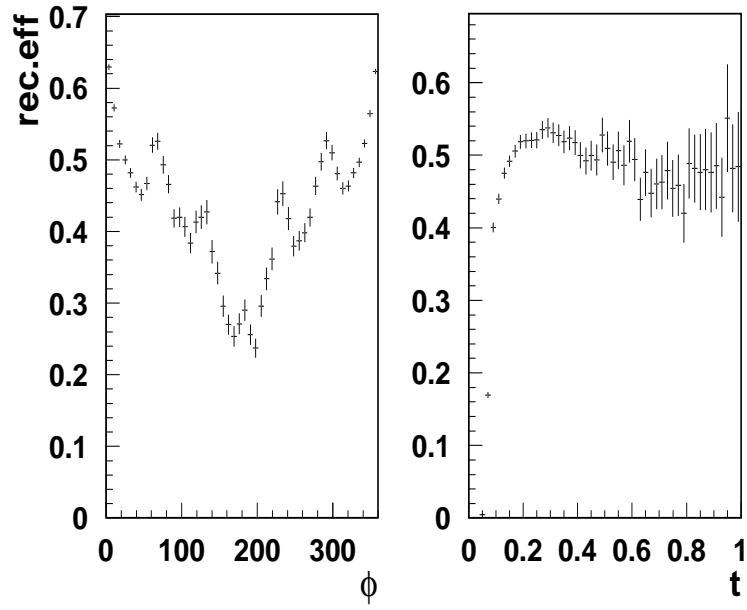


Figure 11: The reconstruction efficiency of DVCS events (epX sample) for $Q^2 > 1.5$ as a function of the azimuthal angle ϕ (left) and t (right). The t -plot has additional cut on $|\phi - \pi| < 2.5\text{rad}$.

enters through the dependence of the inductance of a coil on the susceptibility (χ) of the enclosed sample, $L = L_0[1 + \eta\chi]$, and the constant relating susceptibility to change in inductance, η , is an effective filling factor for the material within the coil. (Essentially, the filling factor is the fraction of the magnetic energy produced by the transmitter coil that falls within the enclosed sample.) The presence of a polarizable sample increases the small mutual inductance coupling the two coils. The susceptibility is a complex valued resonance function, with non-zero value only very near the Larmor frequency, and can be mapped out by sweeping the external magnetic field while applying a fixed RF frequency. The NMR signal from a frozen-spin target after a high-field/low-temperature cycle is quite large. But converting this signal into a polarization requires precise knowledge of the filling factor, η . This must be measured from initial thermal equilibrium data, prior to the high-field/low-temperature cycle, when the relaxation times are short (guaranteeing a precisely calculable polarization) and NMR signals are very small. Noise from a variety of sources generates background under the signals, which must also be determined. The signal from polarized D is only about 1/3 that of H. However, the stoichiometry of the HD molecule and the precisely known ratio of magnetic moments, μ_D/μ_H , allows the deuteron calibration to be calculated from that of the proton, so that in fact only hydrogen thermal equilibrium measurements are necessary. Polarimetry for nuclear targets has been studied extensively at BNL. The systematic uncertainties in HD polarization are about 4% (relative). The largest single factor (contributing 2.8% relative) is the differential uncertainty on the gain of a lock-in amplifier whose scale must be changed by many orders of magnitude between equilibrium-polarization measurements and high-polarization frozen-spin measurements. Separation of signal and background in the calibration measurements contributes at the 1% level.

Additional estimate of the product of target and beam polarizations, $P_B P_T$, will be done also off-line by comparing the well known elastic asymmetry

$$A_{theo} = -\frac{\cos \theta_\gamma \sqrt{1 - \epsilon^2} + (\frac{Q^2}{4M^2})^{-\frac{1}{2}} \sqrt{2\epsilon(1 - \epsilon)} \sin \theta_\gamma \cos \phi_\gamma \frac{G_E}{G_M}}{\epsilon(\frac{Q^2}{4M^2})^{-1} (\frac{G_E}{G_M})^2 + 1} \quad (19)$$

with the measured asymmetry

$$A_{meas} = \frac{N^+ - N^-}{N^+ + N^-} = \frac{P_B P_T \sigma_{et}}{\sigma_0} \equiv P_B P_T A_{theo}. \quad (20)$$

For the ratio $\frac{G_E}{G_M}$, we will use values from polarization transfer measurements [29], which are expected theoretically to have the same (small) two-photon corrections as A_{LT} measurements. On average, the uncertainty in A_{LT} due to G_E/G_M will be about 2% (relative). The measurements will consist of measuring both an electron and a proton, and imposing missing momentum and energy cuts to isolate the elastic channel. Events from H and D will be distinguished through a multi-parameter fit to the missing mass and energy distributions: Fermi broadening in the deuteron

generates peaks that are typically twice as wide as for hydrogen, for the conditions of this proposal (based on the similar conditions in Eg1). Due to this mixing, the errors will be approximately 1.4 times bigger than for targets which contain only H or D plus heavy materials such as nitrogen or aluminum. The projected error on A_{LT} for H from this experiment are shown in Fig. 15. For comparison, the larger A_{LL} asymmetries measured in Eg1 at 5.7 GeV are also shown. Averaged over Q^2 , we expect to determine the product of beam and target polarization, $P_B P_t$, with a relative statistical precision of 3%, and a systematic error of 2%. For the deuteron, we project errors of 7% statistical and 4% systematic. The larger systematic error, relative to the proton, is driven by quasi-elastic modeling uncertainties.

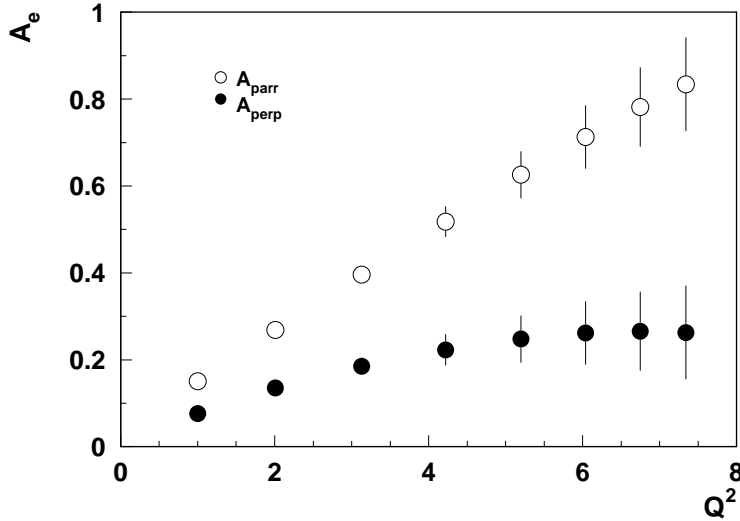


Figure 12: Projected ep elastic asymmetry A_{LT} and corresponding errors for H for this proposal as a function of Q^2 (solid circles). For comparison, A_{LL} asymmetries from Eg1 are also shown.

4.1.5 Trigger and data acquisition

We are planning to use the standard e1 production trigger, data acquisition, and online monitoring system of CLAS. The signal amplitude and time information will be read out using standard ADC and TDC boards currently in use in CLAS. The standard single particle CLAS level 1 trigger will be used to select scattered electrons.

No changes to the trigger hardware are anticipated. Run conditions are listed in the Table 4.1.5.

Table 2: Run conditions.

| | |
|---------------------|---------|
| Beam energy | 6 GeV |
| Beam current | 1-2nA |
| Run time | 30 days |
| Torus current | 2250 |
| Mini torus current | 6000 |
| Target position | -70 cm |
| Mini torus position | -50 cm |
| Target material | HD-Ice |

4.2 Event identification, reconstruction, and acceptances

Electrons are separated from heavier particles using threshold gas Cherenkov counters (CC) and electromagnetic calorimeters, and protons are identified using tracking in the toroidal magnetic field and measurement of time of flight. Charged particle momenta are reconstructed in the CLAS drift chamber system using the standard CLAS reconstruction software.

Standard CLAS particle ID will be used for event identification for $ep \uparrow \rightarrow ep\gamma$ in CLAS. All possible combinations of three final-state particles will be detected. While the electron and proton detection efficiency is fairly large, the $ep\gamma$ events will be fully reconstructed only $\sim 30\%$ of cases. The epX provides the largest sample and is used in most of the projections. The $ep\gamma$ provides the cleanest sample and will be used to check the epX extraction and contamination. The $e\gamma X$ doesn't rely on the detection of the nucleon detection and will be used to compare events from hydrogen and deuteron.

For the proposed experiment, photons from direct production and from π^0 decays (or from η decays) will be reconstructed using the CLAS forward angle electromagnetic calorimeter (EC). The shifted upstream target will provide large acceptance coverage for both reactions.

4.2.1 Separation of single γ from $\gamma\gamma$ events.

Accidental coincidences do not play any significant role in electron scattering experiments with CLAS because of the low luminosity and the good time resolution. The main sources of background to the $ep\gamma$ final state will be from $ep\pi^0$ and from $ep\gamma\gamma$ events, where only one of the two photons is detected.

The $ep\gamma\gamma$ corresponding to hadronic production of two photons, can be measured in the experiment, or inelastic radiative electromagnetic processes. The latter ones

are dominated by processes in which the incoming electron radiates off a photon (which escapes detection in the beam pipe) and, for instance, N^* resonances are excited, which subsequently decay into a proton and a photon. The $\gamma\gamma$ final states appear as a continuum in the epX missing mass, so that most of these events will be eliminated by missing mass cuts. The electromagnetic decay is suppressed by typically two orders of magnitude in comparison to a hadronic process. However, the usual radiative corrections are needed to determine the unradiated cross section.

A significant fraction of $ep\pi^0$ will be detected and used to separate π^0 contributions in $ep\gamma$ and epX samples. These former processes will be measured directly for the same kinematics as the $ep\gamma$ process, and can be subtracted. The contamination from exclusive pions in the DVCS sample $N_\gamma^{Data}(\pi^0)$ will be estimated using the sample of π^0 events and the ratio of efficiencies of single/"0" photon, $N_{0,1\gamma(\pi^0)}^{MC}$, and two photon $N_{\pi^0}^{MC}$ reconstructed π^0 s from the MC :

$$N_{0,1\gamma}^{Data}(\pi^0) = N_{\pi^0}^{Data} \frac{N_{0,1\gamma(\pi^0)}^{MC}}{N_{\pi^0}^{MC}} \quad (21)$$

Even though the missing mass resolution achieved in CLAS with HD-Ice target will be significantly better than for dedicated DVCS experiment using the solenoid target magnet, or the polarized target magnet (see Fig.13) it will not be good enough to separate $ep\gamma$ and $ep\pi^0$ final states event-by-event. The DVCS MC will be used to estimate the contamination from π^0 .

Three different samples of events, epX , $ep\gamma$ and $ep\gamma\gamma$ will be analyzed to separate exclusive $ep\pi^0$ events from DVCS events. It was demonstrated that DVCS asymmetries extracted from e1f and e16 data sets ($E_e \approx 5.7\text{GeV}$) where only epX events were detected, were consistent both with $ep\gamma$ events from the same data sets and also with $ep\gamma$ data set from the dedicated DVCS experiment (e1DVCS) where all 3 final state particles were detected.

The comparison of different samples of DVCS and exclusive π^0 events from 5.7 GeV data (e1f) with MC shows (see Figs.14-17) a very good description of the data, allowing precision estimates of the contamination using the MC for both "0" photon (epX) and single photon DVCS ($ep\gamma$) events.

The total contamination and corresponding efficiency ratios for the e1f data set in one of the bins is shown in Fig.18 and Fig.19 for single photon and "0" photon samples respectively.

The π^0 contamination for exclusive $ep\gamma$ events could be accounted bin by bin using subtraction of ϕ distributions from π^0 from the total count of exclusive photons. The kinematic dependences of measured SSA will be corrected for all bins in x, t, Q^2 and azimuthal angle ϕ . Comparison of subtracted and non-subtracted distributions for some bins using the e1f data are shown in Fig.20 indicating that corrections from π^0 contamination are typically small.

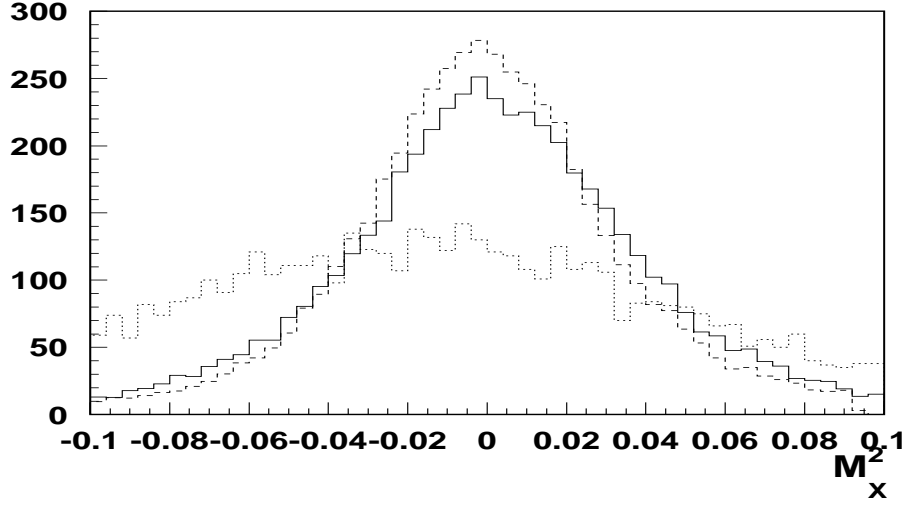


Figure 13: Missing mass (epX) distributions for the HD-Ice (solid line) compared to e1f (dashed) and e1DVCS (dotted) data sets.

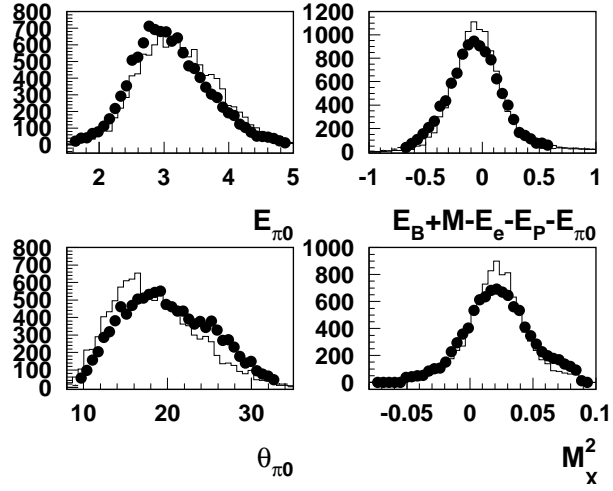


Figure 14: Kinematic distributions of π^0 s from data (filled circles) and MC for $t < 0.6$. All distributions are normalized to the total number of π^0 s.

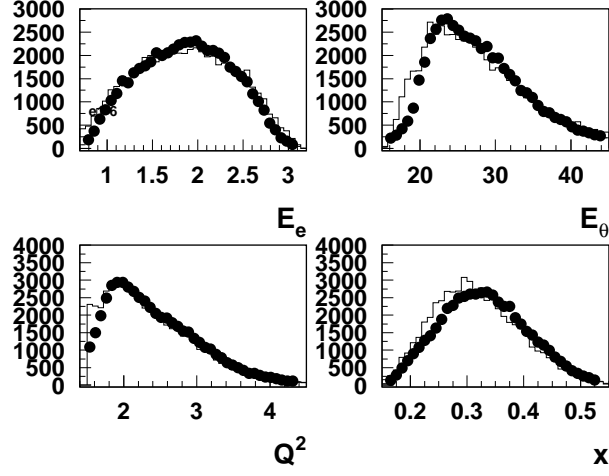


Figure 15: DVCS MC vs data (filled circles) for e1f data set ($ep\gamma$ sample).

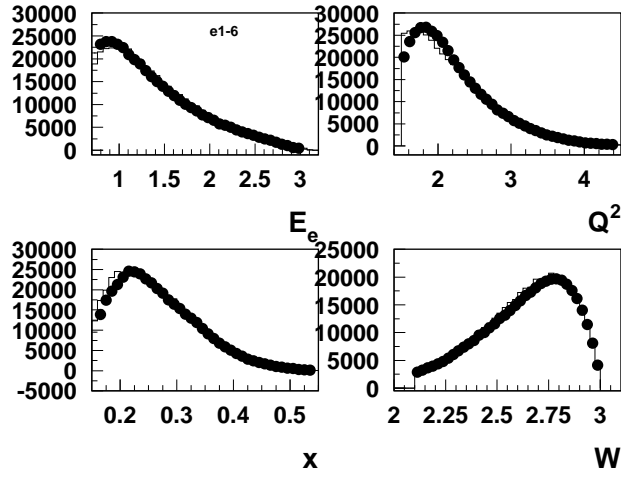


Figure 16: DVCS MC vs data for e16 data set (epX sample).

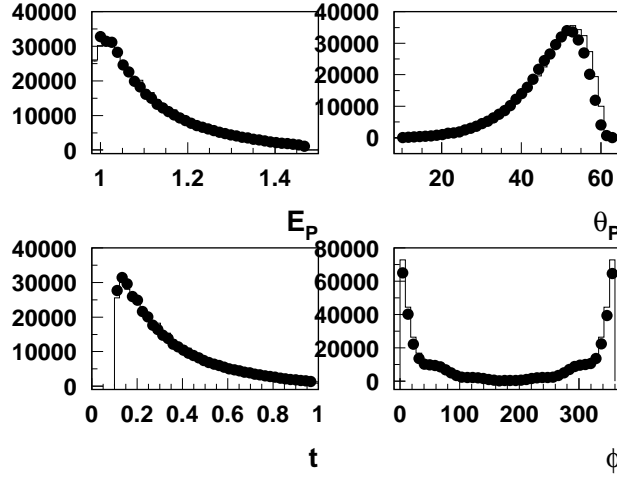


Figure 17: DVCS MC vs data for e1f data set (epX sample).

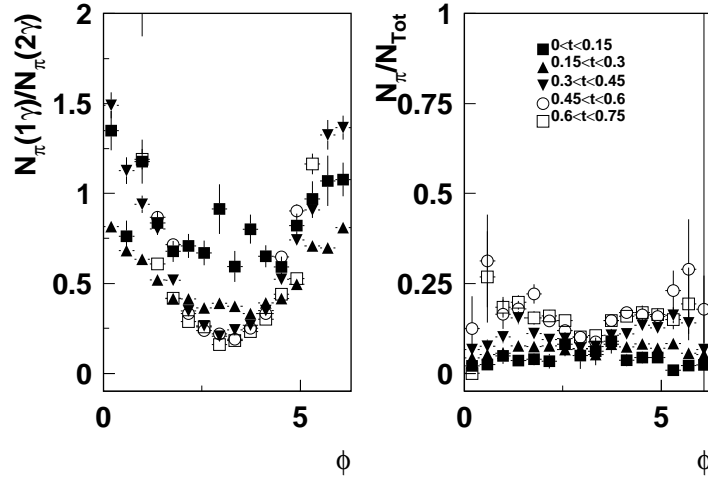


Figure 18: Relative efficiency of reconstruction of single and double photon π^0 events (left) and the fraction of single photons from π^0 s (right) for $ep\gamma$ events ($2.0 < Q^2 < 3.0 \text{ GeV}$ and $0.28 < x < 0.4$)

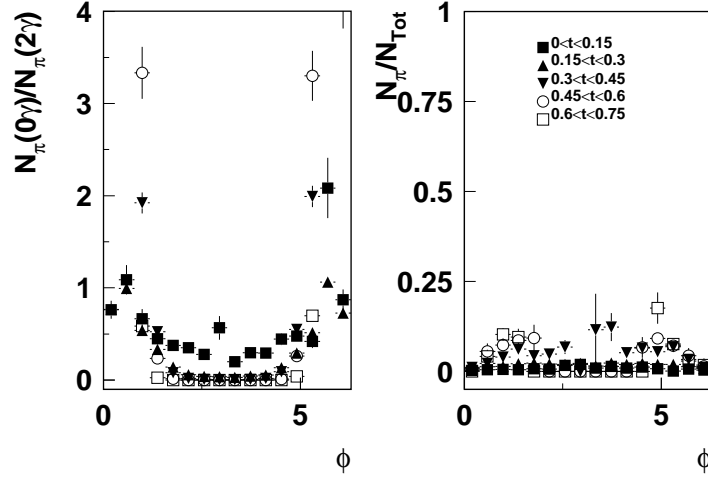


Figure 19: Relative efficiency of reconstruction of 0 and double photon π^0 events (left) and the fraction of single photons from π^0 s (right) for epX events ($2.0 < Q^2 < 3.0 \text{ GeV}$ and $0.28 < x < 0.4$)

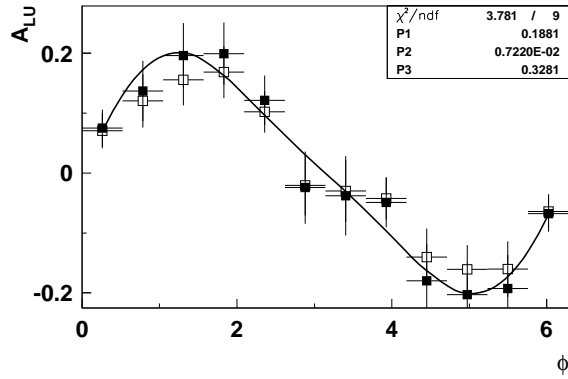


Figure 20: Fits to the azimuthal distributions before (open squares) and after (filled squares) π^0 subtraction for the bin $2.0 < Q^2 < 3.0 \text{ GeV}$ and $0.28 < x < 0.4$

A sample of directly detected photons in the CLAS EC will allow separation of single photons from π^0 s event-by-event. The e1-6 data analysis and the DVCS MC studies with GSIM indicate that single photons can be separated from π^0 s for momenta up to 4 GeV/c by direct reconstruction.

For the DVCS analysis, the reaction $ep \uparrow \rightarrow ep\gamma$ was studied using the MC, and single photon events were separated using the geometrical cut requiring the measured photon to be within a 1° cone relative to the direction calculated of the real photon using the detected scattered electron and the proton.

The DVCS MC with polarized target was used to simulate the angular distributions of photons and π^0 , and to estimate the possible contamination from π^0 in single photon events.

4.2.2 $e\gamma X$ studies

The contamination of photons in the BH-DVCS sample is not very large when the energy of the final state photon is large. That allowed the HERMES collaboration at HERA and the Hall-A collaboration at JLab, to successfully analyze the DVCS-BH asymmetries and cross sections, respectively, while detecting in the final state only the scattered electron and the high energy photon. The missing mass distribution of $e\gamma X$ events, shows a clear peak at the nucleon mass without any additional cuts, when requiring the photon to take more than 60% of the virtual photon energy. The $e\gamma X$ distribution for single photon events for the e1f experiment with similar kinematics is shown in Fig.21. The comparison of curves with and without cuts to separate a clean sample of DVCS events, indicates that the contamination from non BH-DVCS sources is not very significant. The background from different sources, including Δ production and exclusive π^0 production could be estimated using MC, tuned to describe unpolarized data.

The analysis of the $e\gamma X$ data set, thus doesn't involve the detection of the nucleon and is the same for the proton and deuteron targets.

4.3 Count rates and statistical errors

The expected number of counts is given by

$$N = \mathcal{L} \times \text{time} \times \sigma \times (\Delta Q^2 \cdot \Delta x_B) \times \Delta t \times \Delta\phi \times (\Delta\phi_S - \phi)_{\text{eff}}/2\pi \quad (22)$$

With the proposed configuration as described in Sec. 4.1, a luminosity of $5 \times 10^{33} \text{ cm}^{-2}\text{s}^{-1}$ is expected.

The resulting number of DVCS events for the proposed experiment is calculated from the 21 days of the e1f run (same conditions, target position at -25cm) scaled to 25 days. The target polarization is assumed 75% and 25% for hydrogen and deuterium respectively and beam polarization of 0.8 is assumed for the calculation of $\Delta(TDSA)$. All the above factors have been taken into account when calculating the statistical uncertainty.

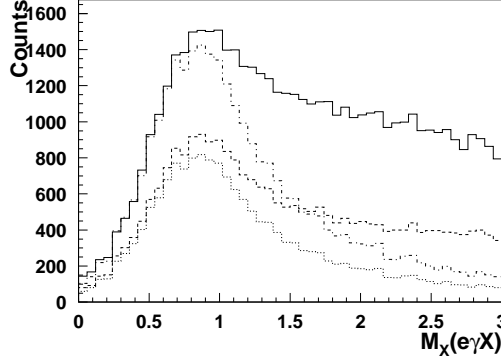


Figure 21: $e\gamma X$ distributions for final state photons with energy above 2.5 GeV from e1f data set with beam energy 5.5 GeV. Solid line has no cuts except $W^2 > 4, Q^2 > 1.5$. The dashed line shows the the same M_X when the proton is detected (50%cases), and the dotted line shows the same M_X when additional angular cut on the photon applied to identify the DVCS event. The dash-dotted line shows the same as the dotted, but scaled to account for the proton reconstruction efficiency.

4.4 Systematic errors

The proposed spin asymmetry measurement is rather insensitive to systematic uncertainties such as charge normalization. The systematic errors can be divided into two categories: those that scale with the measured asymmetry, and those that are independent of the measured results. In the first category, the dominant error is expected to be that from target polarization and the dilution from the unwanted HD and Al backgrounds. For the second category, we have taken our best estimate of the magnitude of the systematic effect, and divided by the average expected proton asymmetry. One of the main contributions to the estimated relative uncertainties, summarized in Table 4.4, comes from the procedure used to separate the azimuthal moments of interest from other, potentially non-zero, azimuthal asymmetries (in total 3-5 different moments depending on ϕ and ϕ_S). Another large contribution is from possible contamination of the single-photon event sample by misidentified photons from π^0 and non-exclusive events. As these events will have a different asymmetry from single photon events they add a systematic error to the asymmetry. The π^0 asymmetry will be measured simultaneously and can thus be corrected for, as the size of the π^0 contamination can be measured as well. From the analysis of the 5.7 GeV e1-6 data we conclude that the $ep(\pi^0)$ yield is generally smaller than the $ep(\gamma)$ yield except for some extreme kinematics where it may be comparable or larger. The uncertainty from radiative corrections is normally small ($\approx 1\%$) based on our previous studies for the e1DVCS,EG1,e1f and e16 experiments.

We conservatively estimate the total systematic error on the asymmetry to be of order 10%, sufficiently small for a very significant measurement.

Table 3: Estimated contributions to the relative systematic uncertainty on the DVCS single spin asymmetry.

| Error source | Systematic error (%) |
|----------------------------|----------------------|
| H/D background | 4 |
| P_t | 5 |
| acceptance corrections | 7 |
| Al background contribution | 3 |
| π^0 contamination | 4 |
| Radiative corrections | 3 |
| Total | ~ 10 |

4.5 Projected results

The measurements with transversely polarized target offer a variety of observables sensitive to different combinations of GPDs. The wide phase space coverage of CLAS will allow to bin observables in different bins for relevant kinematical variable, so shown below are few projections for representative measurements. The corresponding projections for CLAS data set based on 25 days of HD data taking are shown in Fig. 22 and Fig. 23, respectively, and for few different values of the total quark angular momenta J_u, J_d .

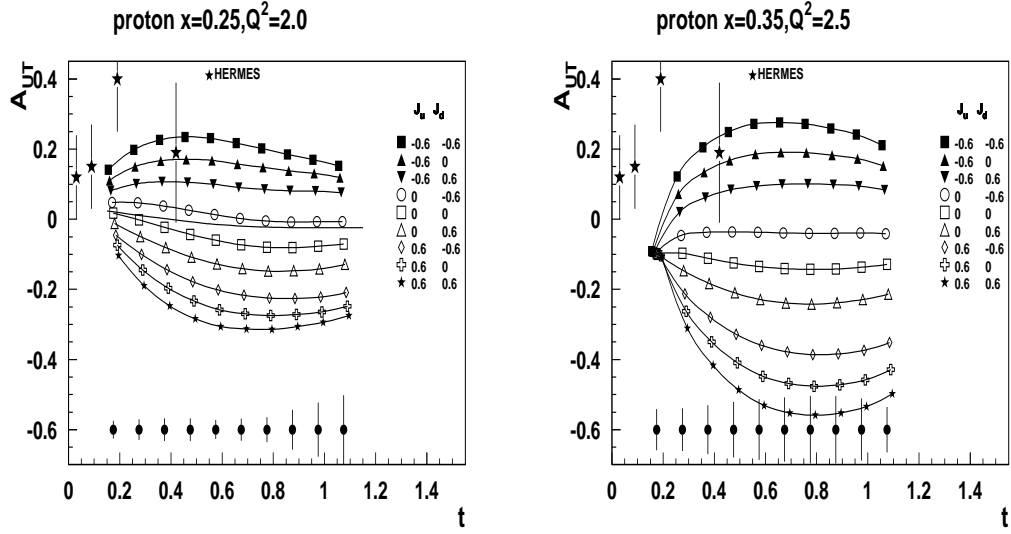


Figure 22: Expected DVCS TTSA amplitudes $A_{UT}^{\sin(\phi-\phi_S)\cos\phi}$ as a function of t , using the dual parameterization for GPDs H and E [25] ($\tilde{\mathcal{H}} = \tilde{\mathcal{E}} = 0$). The projected statistical error for 25 days with hydrogen polarization 75% (2 bins in x, Q^2) is shown. The solid line (extending to $t=1.3$) on the left plot corresponds to the case $E=0$. The systematic error is expected to not exceed the statistical one.

The variation of the asymmetries (TTSA and TDSA) as a function of the relevant kinematic variables according to different models of GPDs [23] are shown in the following figures:

- Figure 24 shows the ϕ dependence of the target SSA.
- Figure 25 shows the t dependence of the double spin asymmetries (DSA or A_{LT}).

High precision data over a large phase space will allow us to constrain the quark angular momentum in the proton, J_q . While not fully model-independent, this method of extracting J_q will become more and more accurate as amplitude calculations and

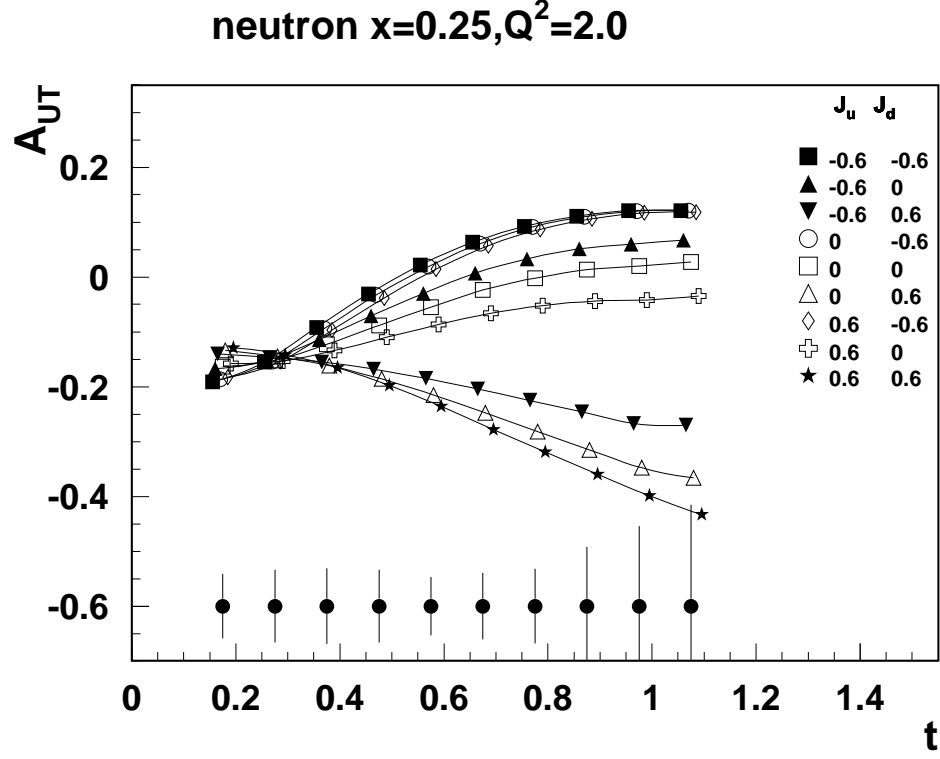


Figure 23: Expected DVCS TTSA amplitudes $A_{UT}^{\sin(\phi-\phi_S)\cos\phi}$ as a function of t , using the dual parameterization [25]. The projected statistical error for 25 days with deuteron polarization 25% is shown. The systematic error is expected to not exceed the statistical one.

GPD parameterizations become more refined as a result of measurements of a variety of other DVCS and meson production observables.

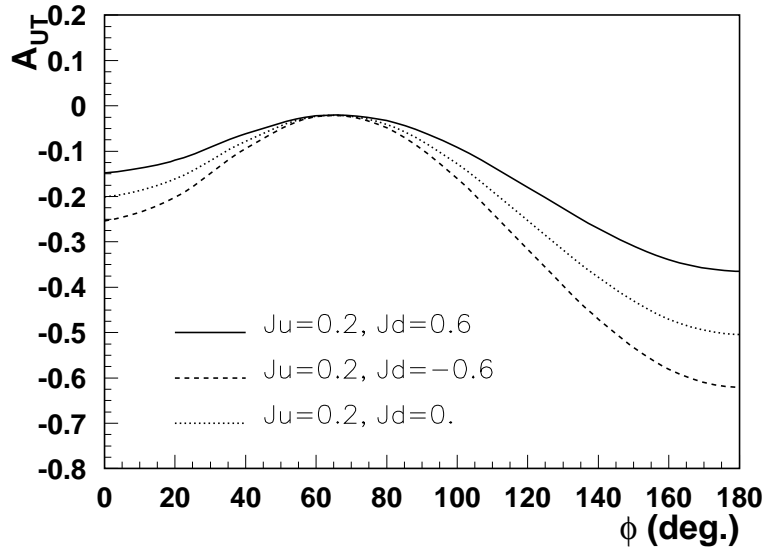


Figure 24: Expected DVCS A_{UT} in the Regge ansatz for $b_{val} = 1$, $b_{sea} = 1$, $J_u = 0.2$, $J_d = -0.6, 0.0, 0.6$ as a function of azimuthal angle ϕ using the VGG formalism [23]. The calculations are done at the average kinematic values $Q^2 = 2.2$, $x_B = 0.34$, $t = 0.55$. Projected statistical errors are shown.

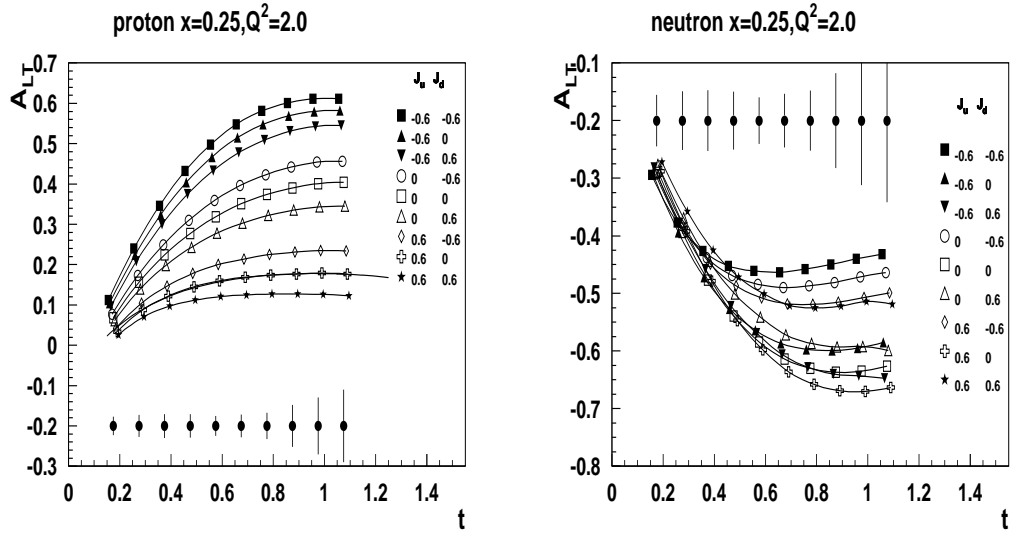


Figure 25: Expected DVCS TDSA amplitudes A_{LT} as a function of t , using the the dual parameterization for GPDs H and E [25]. The projected statistical error for transversely polarized hydrogen (left) and neutron (right). The solid line (extending to $t=1.3$) on the left plot corresponds to the case $E=0$. The systematic error is expected to not exceed the statistical one.

5 Summary and beam time request

In this experiment we propose a study of the Generalized Parton Distributions (GPD) via measurements of Deeply Virtual Compton Scattering in the hard scattering kinematics ($Q^2 > 1\text{GeV}^2$, $W^2 > 4\text{GeV}^2$), using a 6 GeV electron beam and the CLAS detector. The experiment will use CLAS with the transversely polarized HD-Ice target shifted upstream to provide wider acceptance for DVCS photons. For this proposal, we request 30 days of beam time with high polarization of electrons at 6 GeV and a transversely polarized polarized hydrogen target (25 HD, 5 days calibration runs including H, D and empty targets). We expect to improve both the systematic (~ 2) and statistical (~ 4) uncertainties of HERMES measurements at large x ($x > 0.2$), and also obtain first data with transversely polarized deuterium.

The DVCS process will be determined via interference with the Bethe-Heitler process by measuring the transverse target spin asymmetry (TTSA). This asymmetry is directly comparable to calculations and predictions in terms of magnitude, Q^2 , x_B and t behaviors. Combined with future measurements at higher energies the 6 GeV data will provide kinematical coverage for Q^2 -dependence studies at fixed x , important for understanding of higher twist corrections to DVCS asymmetries.

We believe that the measurements that we intend to carry out in this proposal will provide important information on GPD-E, crucial for understanding of the structure of the nucleon in terms of GPDs. This kind of study involves a simultaneous scan of various variables (x_B , Q^2 , t), so a large acceptance detector such as CLAS is most suitable. Analysis of already existing electro-production data from CLAS with unpolarized and longitudinally polarized targets have shown that the proposed measurements are feasible. Combined analysis of all three data sets will allow for the first time to perform a model independent separation of different GPD contributions.

The open acceptance configuration with HD-Ice target compared to previous runs with polarized targets (EG1,EG1dvcs), combined with increased compared to e16 and e1f data sets acceptance for direct photons ($> 40\%$, variable with kinematics), will allow us to extend to large x measurements with transversely polarized hydrogen and perform first measurements with transversely polarized deuterium target.

Beam Request

We ask the PAC to award 30 days of beam time for a dedicated high statistics DVCS experiment with the transversely polarized target.

No new equipment is involved and the experiment could be ready after tests with HD-Ice target will verify polarization retention with electron beam.

The proposed DVCS measurement with CLAS will provide stringent constraints on models for GPDs. Precision data for the DVCS process at 6 GeV with transversely po-

larized hydrogen and deuterium will make significant contribution in our understanding of spatial distributions of quarks and their orbital angular momentum together with independent measurements related to spin-orbit correlations and transversity distribution will help to construct a more complete picture of the nucleon in terms of elementary quarks and gluons going beyond the simple collinear partonic representation. Global analysis of DVCS data will also help maintain the momentum in the theory community providing important support for future measurements with upgraded to 12 GeV JLab.

APPENDIX A: Extraction of CFFs

CFFs using measured azimuthal moments $c_{1,A}^{\mathcal{I}}$ and $s_{1,A}^{\mathcal{I}}$ are defined as [6]:

$$\mathcal{H} = \frac{2 - x_B}{(1 - x_B)D} \left\{ \left[\left(2 - x_B + \frac{4x_B^2 M^2}{(2 - x_B)\Delta^2} \right) F_1 + \frac{x_B^2}{2 - x_B} F_2 \right] \mathcal{C}_{\text{unp}}^{\mathcal{I}} \right. \\ \left. - (F_1 + F_2) \left[x_B \mathcal{C}_{\text{LP}}^{\mathcal{I}} + \frac{2x_B^2 M^2}{(2 - x_B)\Delta^2} (x_B \mathcal{C}_{\text{LP}}^{\mathcal{I}} - \mathcal{C}_{\text{TP}+}^{\mathcal{I}}) \right] + F_2 \mathcal{C}_{\text{TP}-}^{\mathcal{I}} \right\}, \quad (23)$$

$$\mathcal{E} = \frac{2 - x_B}{(1 - x_B)D} \left\{ \left[4 \frac{1 - x_B}{2 - x_B} F_2 - \frac{4M^2 x_B^2}{(2 - x_B)\Delta^2} F_1 \right] \mathcal{C}_{\text{unp}}^{\mathcal{I}} + \frac{4x_B M^2}{(2 - x_B)\Delta^2} (F_1 + F_2) \right. \\ \left. \times (x_B \mathcal{C}_{\text{LP}}^{\mathcal{I}} - \mathcal{C}_{\text{TP}+}^{\mathcal{I}}) + \frac{4M^2}{\Delta^2} F_1 \mathcal{C}_{\text{TP}-}^{\mathcal{I}} \right\}, \quad (24)$$

$$\tilde{\mathcal{H}} = \frac{2 - x_B}{(1 - x_B)D} \left\{ (2 - x_B) F_1 \mathcal{C}_{\text{LP}}^{\mathcal{I}} - x_B (F_1 + F_2) \mathcal{C}_{\text{unp}}^{\mathcal{I}} + \left[\frac{2x_B M^2}{\Delta^2} F_1 + F_2 \right] \right. \\ \left. \times (x_B \mathcal{C}_{\text{LP}}^{\mathcal{I}} - \mathcal{C}_{\text{TP}+}^{\mathcal{I}}) \right\}, \quad (25)$$

$$\tilde{\mathcal{E}} = \frac{2 - x_B}{(1 - x_B)D} \left\{ \frac{4M^2}{\Delta^2} (F_1 + F_2) (x_B \mathcal{C}_{\text{unp}}^{\mathcal{I}} + \mathcal{C}_{\text{TP}-}^{\mathcal{I}}) + \left[4 \frac{1 - x_B}{x_B} F_2 - \frac{4x_B M^2}{\Delta^2} F_1 \right] \right. \\ \left. - \frac{4(2 - x_B)M^2}{x_B \Delta^2} F_1 \mathcal{C}_{\text{TP}+}^{\mathcal{I}} \right\}, \quad (26)$$

where

$$D = 4 \left(F_1^2 - \frac{\Delta^2}{4M^2} F_2^2 \right) \left(1 - \frac{\Delta_{\text{min}}^2}{\Delta^2} \right).$$

The real and imaginary parts of $\mathcal{C}_A^{\mathcal{I}}$ are defined by corresponding $\cos(\phi)$ and $\sin(\phi)$ moments of the interference term ($c_{1,A}^{\mathcal{I}}$ and $s_{1,A}^{\mathcal{I}}$). The CFFs \mathcal{E} and $\tilde{\mathcal{E}}$ are dominated by azimuthal moments $s_{1,TP\pm}^{\mathcal{I}}$ and $c_{1,TP\pm}^{\mathcal{I}}$ accessible only with transversely polarized target.

APPENDIX B: Transverse target asymmetries

Expression for A_{UT}

The general expression for the A_{UT} asymmetry reads [6]:

$$A_{UT}(\phi) = \frac{\mathcal{I}_{\text{TP}}(\varphi, \phi) + |\mathcal{T}_{\text{TP}}^{\text{DVCS}}(\varphi, \phi)|^2}{|\mathcal{T}_{\text{unp}}^{\text{BH}}(\phi)|^2 + \mathcal{I}_{\text{unp}}(\phi) + |\mathcal{T}_{\text{unp}}^{\text{DVCS}}(\phi)|^2} \quad (27)$$

where the angle $\varphi = \phi_S - \phi$.

The different contributions (for electron beam) are

$$\begin{aligned}
\mathcal{I}_{\text{TP}}(\varphi, \phi) &= \frac{-e^6}{x_B y^3 t P_1(\phi) P_2(\phi)} (c_{0,\text{TP}}^{\mathcal{I}} + c_{1,\text{TP}}^{\mathcal{I}} \cos \phi + c_{2,\text{TP}}^{\mathcal{I}} \cos 2\phi \\
&\quad + s_{1,\text{TP}}^{\mathcal{I}} \sin \phi + s_{2,\text{TP}}^{\mathcal{I}} \sin 2\phi), \\
|\mathcal{T}_{\text{TP}}^{\text{DVCS}}(\varphi, \phi)|^2 &= \frac{e^6}{y^2 Q^2} (c_{0,\text{TP}}^{\text{DVCS}} + c_{1,\text{TP}}^{\text{DVCS}} \cos \phi + s_{1,\text{TP}}^{\text{DVCS}} \sin \phi), \\
|\mathcal{T}_{\text{unp}}^{\text{BH}}(\varphi, \phi)|^2 &= \frac{e^6}{x_B^2 y^2 t P_1(\phi) P_2(\phi) (1 + \epsilon^2)^2} (c_{0,\text{unp}}^{\text{BH}} + c_{1,\text{unp}}^{\text{BH}} \cos \phi + c_{2,\text{unp}}^{\text{BH}} \cos 2\phi), \\
\mathcal{I}_{\text{unp}}(\varphi, \phi) &= \frac{-e^6}{x_B y^3 t P_1(\phi) P_2(\phi)} (c_{0,\text{unp}}^{\mathcal{I}} + c_{1,\text{unp}}^{\mathcal{I}} \cos \phi + c_{2,\text{unp}}^{\mathcal{I}} \cos 2\phi), \\
|\mathcal{T}_{\text{unp}}^{\text{DVCS}}(\varphi, \phi)|^2 &= \frac{e^6}{y^2 Q^2} (c_{0,\text{unp}}^{\text{DVCS}} + c_{1,\text{unp}}^{\text{DVCS}} \cos \phi). \tag{28}
\end{aligned}$$

In the above expressions, the leading twist harmonics are $c_0^{\mathcal{I}}$, $c_1^{\mathcal{I}}$ and $s_1^{\mathcal{I}}$ for the interference term, c_0^{DVCS} for the DVCS squared term and all harmonics for the BH squared term (the latter is calculated exactly without the twist expansion).

For the transversely polarized target, all harmonics also depend on the angle φ . In particular, for the *unpolarized* beam, one has

$$\begin{aligned}
c_{n,\text{TP}}^{\mathcal{I}} &= \tilde{c}_{n,\text{TP}}^{\mathcal{I}} \sin \varphi \\
s_{n,\text{TP}}^{\mathcal{I}} &= \tilde{s}_{n,\text{TP}}^{\mathcal{I}} \cos \varphi \\
c_{n,\text{TP}}^{\text{DVCS}} &= \tilde{c}_{n,\text{TP}}^{\text{DVCS}} \sin \varphi \\
s_{1,\text{TP}}^{\text{DVCS}} &= \tilde{s}_{1,\text{TP}}^{\text{DVCS}} \cos \varphi \tag{29}
\end{aligned}$$

We are interested in the harmonics proportional to $\sin \varphi$ since we want to separate GPDs H and E from the GPDs \tilde{H} and \tilde{E} , which drive the harmonics proportional to $\cos \varphi$. Therefore, the $\sin \varphi$ -moment of A_{UT} is

$$A_{UT}^{\sin \varphi}(\phi) = \frac{\tilde{\mathcal{I}}_{\text{TP}}(\varphi, \phi) + |\tilde{\mathcal{T}}_{\text{TP}}^{\text{DVCS}}(\varphi, \phi)|^2}{|\mathcal{T}_{\text{unp}}^{\text{BH}}(\phi)|^2 + \mathcal{I}_{\text{unp}}(\phi) + |\mathcal{T}_{\text{unp}}^{\text{DVCS}}(\phi)|^2}, \tag{30}$$

where

$$\begin{aligned}
\tilde{\mathcal{I}}_{\text{TP}}(\varphi, \phi) &= \frac{-e^6}{x_B y^3 t P_1(\phi) P_2(\phi)} (\tilde{c}_{0,\text{TP}}^{\mathcal{I}} + \tilde{c}_{1,\text{TP}}^{\mathcal{I}} \cos \phi + \tilde{c}_{2,\text{TP}}^{\mathcal{I}} \cos 2\phi), \\
|\tilde{\mathcal{T}}_{\text{TP}}^{\text{DVCS}}(\varphi, \phi)|^2 &= \frac{e^6}{y^2 Q^2} (\tilde{c}_{0,\text{TP}}^{\text{DVCS}} + \tilde{c}_{1,\text{TP}}^{\text{DVCS}} \cos \phi) \tag{31}
\end{aligned}$$

These harmonics are

$$\begin{aligned}
\tilde{c}_{0,\text{TP}}^{\mathcal{I}} &= \frac{8m_N\sqrt{1-y}K}{Q}(2-y)\Im m \left\{ \frac{(2-y)^2}{1-y} C_{\text{TP}-}^{\mathcal{I}}(\mathcal{F}) + \Delta C_{\text{TP}-}^{\mathcal{I}}(\mathcal{F}) \right\}, \\
\tilde{c}_{1,\text{TP}}^{\mathcal{I}} &= \frac{8m_N\sqrt{1-y}}{Q}(2-2y+y^2)\Im m C_{\text{TP}-}^{\mathcal{I}}(\mathcal{F}), \\
\tilde{c}_{2,\text{TP}}^{\mathcal{I}} &= \frac{16m_N\sqrt{1-y}K}{Q(2-x_B)}(2-y)\Im m C_{\text{TP}-}^{\mathcal{I}}(\mathcal{F}^{\text{eff}}), \\
\tilde{c}_{0,\text{TP}}^{\text{DVCS}} &= -\frac{QK}{m_N\sqrt{1-y}}(2-2y+y^2)\Im m C_{\text{TP}-}^{\text{DVCS}}(\mathcal{F}, \mathcal{F}^*), \\
\tilde{c}_{1,\text{TP}}^{\text{DVCS}} &= -\frac{4QK^2}{m_N(2-x_B)\sqrt{1-y}}(2-y)\Im m C_{\text{TP}-}^{\text{DVCS}}(\mathcal{F}^{\text{eff}}, \mathcal{F}^*)
\end{aligned} \tag{32}$$

In the expressions above (ignoring the GPDs \tilde{H} and \tilde{E} and the dynamical twist-three contributions to the GPDs H and E),

$$\begin{aligned}
C_{\text{TP}-}^{\mathcal{I}}(\mathcal{F}) &= \frac{1}{2-x_B} \left(x_B^2 F_1 - (1-x_B) \frac{t}{m_N^2} F_2 \right) \mathcal{H} \\
&\quad + \left\{ \frac{t}{4m_N^2} \left((2-x_B) F_1 + \frac{x_B^2}{2-x_B} F_2 \right) + \frac{x_B^2}{2-x_B} F_1 \right\} \mathcal{E}, \\
\Delta C_{\text{TP}-}^{\mathcal{I}}(\mathcal{F}) &= \frac{t}{m_N^2} (F_2 \mathcal{H} - F_1 \mathcal{E}), \\
C_{\text{TP}-}^{\mathcal{I}}(\mathcal{F}^{\text{eff}}) &= -x_B C_{\text{TP}-}^{\mathcal{I}}(\mathcal{F}), \\
C_{\text{TP}-}^{\text{DVCS}}(\mathcal{F}, \mathcal{F}^*) &= \frac{2}{2-x_B} (\mathcal{H} \mathcal{E}^* - \mathcal{E} \mathcal{H}^*), \\
C_{\text{TP}-}^{\text{DVCS}}(\mathcal{F}^{\text{eff}}, \mathcal{F}^*) &= -x_B C_{\text{TP}-}^{\text{DVCS}}(\mathcal{F}, \mathcal{F}^*)
\end{aligned} \tag{33}$$

The $\cos \phi$ moment of $A_{UT}^{\sin \varphi \cos \phi}$ reads

$$A_{UT}^{\sin \varphi \cos \phi} = \frac{1}{\pi} \int_0^{2\pi} d\phi \cos \phi A_{UT}^{\sin \varphi}(\phi) \tag{34}$$

Expression for A_{LT}

The expression for the A_{LT} asymmetry is given by

$$A_{LT}(\phi) = \frac{|\mathcal{T}_{\text{TP}}^{\text{BH}}(\varphi, \phi)|^2 + \mathcal{I}_{\text{TP}}(\varphi, \phi) + |\mathcal{T}_{\text{TP}}^{\text{DVCS}}(\varphi, \phi)|^2}{|\mathcal{T}_{\text{unp}}^{\text{BH}}(\phi)|^2 + \mathcal{I}_{\text{unp}}(\phi) + |\mathcal{T}_{\text{unp}}^{\text{DVCS}}(\phi)|^2}, \tag{35}$$

where

$$|\mathcal{T}_{\text{TP}}^{\text{BH}}(\varphi, \phi)|^2 = \frac{e^6}{x_B^2 y^2 t P_1(\phi) P_2(\phi) (1+\epsilon^2)^2} (c_{0,\text{TP}}^{\text{BH}} + c_{1,\text{TP}}^{\text{BH}} \cos \phi + s_{1,\text{TP}}^{\text{BH}} \sin \phi) \tag{36}$$

The other expressions for the transversely polarized interference and the DVCS term and for the unpolarized contributions are the same as before.

As in the case of A_{UT} , we are interested in the $\sin \phi$ moment of the asymmetry,

$$A_{LT}^{\sin \phi}(\phi) = \frac{|\tilde{\mathcal{T}}_{\text{TP}}^{\text{BH}}(\varphi, \phi)|^2 + \tilde{\mathcal{I}}_{\text{TP}}(\varphi, \phi) + |\tilde{\mathcal{T}}_{\text{TP}}^{\text{DVCS}}(\varphi, \phi)|^2}{|\mathcal{T}_{\text{unp}}^{\text{BH}}(\phi)|^2 + \mathcal{I}_{\text{unp}}(\phi) + |\mathcal{T}_{\text{unp}}^{\text{DVCS}}(\phi)|^2}. \quad (37)$$

However, the expressions for the numerator are different since the beam polarization projects out the $\sin \phi$ harmonics

$$\begin{aligned} |\tilde{\mathcal{T}}_{\text{TP}}^{\text{BH}}(\varphi, \phi)|^2 &= \frac{e^6}{x_B^2 y^2 t P_1(\phi) P_2(\phi) (1 + \epsilon^2)^2} \tilde{s}_{1,\text{TP}}^{\text{BH}} \sin \phi, \\ \tilde{\mathcal{I}}_{\text{TP}}(\varphi, \phi) &= \frac{-e^6}{x_B y^3 t P_1(\phi) P_2(\phi)} (\tilde{s}_{1,\text{TP}}^{\mathcal{I}} \sin \phi + \tilde{s}_{2,\text{TP}}^{\mathcal{I}} \sin 2\phi), \\ |\tilde{\mathcal{T}}_{\text{TP}}^{\text{DVCS}}(\varphi, \phi)|^2 &= \frac{e^6}{y^2 Q^2} \tilde{s}_{1,\text{TP}}^{\text{DVCS}} \sin \phi \end{aligned} \quad (38)$$

For the *polarized* beam, in the Fourier coefficients, we keep the parts proportional to the polarization λ

$$\begin{aligned} \tilde{s}_{1,\text{TP}}^{\text{BH}} &= 16 y x_B^2 \sqrt{1 - y - \frac{\epsilon^2 y^2}{4} \frac{m_N}{Q}} \sqrt{(1 + \epsilon^2)^3} \left(1 - \frac{t}{Q^2}\right) (F_1 + F_2) \left(F_1 + \frac{t}{4m_N^2} F_2\right), \\ \tilde{s}_{1,\text{TP}}^{\mathcal{I}} &= \frac{8m_N \sqrt{1 - y}}{Q} y(2 - y) \Re C_{\text{TP}-}^{\mathcal{I}}(\mathcal{F}), \\ \tilde{s}_{2,\text{TP}}^{\mathcal{I}} &= \frac{16m_N \sqrt{1 - y} K}{Q(2 - x_B)} y \Re C_{\text{TP}-}^{\mathcal{I}}(\mathcal{F}^{\text{eff}}), \\ \tilde{s}_{1,\text{TP}}^{\text{DVCS}} &= 0. \end{aligned} \quad (39)$$

The fact that $\tilde{s}_{1,\text{TP}}^{\text{DVCS}} = 0$ is because $C_{\text{TP}-}^{\text{DVCS}}$ does not have a real part. Therefore, the DVCS term does not contribute to the numerator of A_{LU} .

The observable of interest is the $\sin \phi$ moment of $A_{LT}^{\sin \phi}(\phi)$,

$$A_{LT}^{\sin \phi \sin \phi} = \frac{1}{\pi} \int_0^{2\pi} d\phi \sin \phi A_{LT}^{\sin \phi}(\phi) \quad (40)$$

- The above moment is used in projection plots as A_{LT} .

References

- [1] D. Mueller et al., Fortschr. Phys. 42 (1994) 101, hep-ph/9812448.
- [2] X.D. Ji, Phys. Rev. D55 (1997) 7114, hep-ph/9609381.
- [3] X.D. Ji, Phys. Rev. Lett. 78 (1997) 610, hep-ph/9603249.
- [4] A.V. Radyushkin, Phys. Lett. B380 (1996) 417, hep-ph/9604317.
- [5] A.V. Radyushkin, Phys. Rev. D56 (1997) 5524, hep-ph/9704207.
- [6] A.V. Belitsky, D. Mueller and A. Kirchner, Nucl. Phys. B629 (2002) 323, hep-ph/0112108.
- [7] Jefferson Lab Hall A, C. Munoz Camacho et al., Phys. Rev. Lett. 97 (2006) 262002, nucl-ex/0607029.
- [8] CLAS, S. Chen et al., Phys. Rev. Lett. 97 (2006) 072002, hep-ex/0605012.
- [9] HERMES, Z. Ye, (2006), hep-ex/0606061.
- [10] F. Ellinghaus et al., Eur. Phys. J. C46 (2006) 729, hep-ph/0506264.
- [11] Jefferson Lab Hall A, M. Mazouz et al., (2007), arXiv:0709.0450 [nucl-ex].
- [12] CLAS, . A.Sandorfi et al., CLAS proposal E06-101 (2006).
- [13] M.V. Polyakov, Phys. Lett. B555 (2003) 57, hep-ph/0210165.
- [14] D.Y. Ivanov et al., Phys. Lett. B550 (2002) 65, hep-ph/0209300.
- [15] D.Y. Ivanov et al., Phys. Part. Nucl. 35 (2004) S67, hep-ph/0401157.
- [16] R. Enberg, B. Pire and L. Szymanowski, Eur. Phys. J. C47 (2006) 87, hep-ph/0601138.
- [17] S. Liuti et al., Proceedings of HADRON-2007 (2007), arXiv:0709.3020 [hep-ph].
- [18] QCDSF, M. Gockeler et al., Phys. Rev. Lett. 98 (2007) 222001, hep-lat/0612032.
- [19] M. Diehl and P. Hagler, Eur. Phys. J. C44 (2005) 87, hep-ph/0504175.
- [20] S. Meissner, A. Metz and K. Goeke, Phys. Rev. D76 (2007) 034002, hep-ph/0703176.
- [21] P.J. Mulders and R.D. Tangerman, Nucl. Phys. B461 (1996) 197, hep-ph/9510301.

- [22] M. Burkardt and D.S. Hwang, Phys. Rev. D69 (2004) 074032, hep-ph/0309072.
- [23] M. Vanderhaeghen, P.A.M. Guichon and M. Guidal, Phys. Rev. D60 (1999) 094017, hep-ph/9905372.
- [24] A.V. Belitsky and D. Mueller, Phys. Lett. B513 (2001) 349, hep-ph/0105046.
- [25] V. Guzey and T. Teckentrup, Phys. Rev. D74 (2006) 054027, hep-ph/0607099.
- [26] F.X. Girod, R.A. Niyazov and f.t.C. collaboration, (2007), arXiv:0711.4805 [hep-ph].
- [27] E143, K. Abe et al., Phys. Rev. D58 (1998) 112003, hep-ph/9802357.
- [28] C. Thorn and . Caracappa, AIP Conf. Proc. (2007) (in press).
- [29] Jefferson Lab Hall A, M.K. Jones et al., Phys. Rev. Lett. 84 (2000) 1398, nucl-ex/9910005.